Lunar Low-Titanium Magmatism during Ancient Expansion inferred from Ejecta originating from Linear Gravity Anomalies

G. Nishiyama[1,2], T. Morota[1], N. Namiki[1,2,3], K. Inoue[1], S. Sugita[1]

[1] The Department of Earth and Planetary Science, The University of Tokyo, Tokyo, Japan.

[2] National Astronomical Observatory of Japan, Mitaka, Japan.

[3] The Graduate University for Advanced Studies, SOKENDAI, Hayama, Japan.

Corresponding author: Gaku Nishiyama (gaku.nishiyama@grad.nao.ac.jp)

Key Points:

- Magma composition during lunar ancient expansion is investigated with spectrum and gravity around craters on linear gravity anomalies.
- High-calcium pyroxene exposures and gravity reduction around Roche crater imply an excavation of subsurface ancient dikes.
- Subsurface dikes formed during the expansion stage are estimated to be composed of low-titanium magma.

Abstract

Linear gravity anomalies (LGAs) on the Moon have been interpreted as ancient magmatic intrusions formed during the lunar expansion. The composition of such ancient subsurface intrusions may offer a hint for the lunar thermodynamic state in the initial stage of lunar history. To pose a first compositional constraint on magmatism related to lunar expansion, this study analyzed the spectrum and gravity around craters on LGAs, such as Rowland, Roche, and Edison craters. Using spectral datasets around the craters, we first surveyed non-mare basaltic exposures that we hypothesize originate from subsurface intrusions. This hypothesis is then investigated in comparison between the GRAIL data and post-cratering gravity simulated with the iSALE shock physics code. Our spectral analysis reveals no basaltic exposure around Rowland crater. Further, the observed termination of LGA at the crater rim contradicts the gravity simulation which assumes that LGA predates Rowland crater. These results suggest that LGA formation postdates the Rowland formation and that lunar expansion lasted even after the Nectarian age. On the other hand, we found that both Roche and Edison craters possess basaltic exposures in their peripheries. Because the gravity reduced inside Roche crater can be reproduced in our simulation, the discovered basaltic exposures are possibly LGA materials ejected from these craters. The composition of those exposures suggests that the LGA intrusions are composed of low-titanium magma. This indicates that ancient magma during the expansion did not contain ilmenite-rich melt provided by a plume ascending from the ilmenite-bearing layer above the core.

Plain Language Summary

The Moon has positive, narrow, and long gravity anomalies, so-called linear gravity anomalies (LGAs), which are believed to be ancient magmatic intrusions formed during the lunar ancient expansion. The composition of these intrusions could provide insights into the early lunar thermal state. In this study, we analyzed the spectra and gravity data around craters located on LGAs, specifically Rowland, Roche, and Edison craters, which might have ejected the LGA material. By analyzing the spectral data, we first identified non-mare basaltic exposures that likely originate from these subsurface formations. We next examine if these exposures are composed of the LGA materials, by comparing the observed data with a simulation of gravity after cratering events. We found no basaltic exposures around Rowland and that gravity inside Rowland is not consistent with the excavation hypothesis, suggesting that LGA formation and lunar expansion occurred after the Rowland formation. On the other hand, we discovered basaltic exposures around both Roche and Edison craters. The gravity inside Roche crater manifests that the discovered basaltic exposures were ejected from the LGAs. The composition of these exposures indicates that LGAs are composed of low-titanium magma, which provides a new constraint on the ancient thermal state of the Moon.

1 Introduction

The early expansion stage of the Moon following its formation is a key to understanding the thermal evolution of the lunar interior. Many lunar evolutionary models have suggested that the Moon might have an expansion state in its thermal history (Laneuville et al., 2013; U et al., 2022; N. Zhang et al., 2013a, 2013b). Petrological studies have indicated that the Moon had a layer of ilmenite-bearing cumulates (IBC) between its anorthositic crust and olivine-

orthopyroxene mantle immediately after solidifying the lunar magma ocean (Elkins-Tanton et al., 2011; Snyder et al., 1992). It has been hypothesized that this dense layer drove a gravitational instability and consequently a mantle overturn, releasing gravitational potential into heat. The overturn could simultaneously transport heat-producing elements to the lunar core-mantle boundary zone, producing radiogenic heat in the deep area of the Moon (e.g., Hess & Parmentier, 1995). The following rise of the lunar temperature may have caused thermal expansion of the lunar volume in the early stage of the Moon (Laneuville et al., 2013; Zhang et al., 2013a, 2013b). This process coincides with melt generation and migration, which could also play a crucial role in the lunar volumetric change (U et al., 2022). The duration of lunar radius change depends on the initial thermal state and lunar inner structures. Thus, temporal constraints on ancient lunar expansion are essential hints to elucidate thermal history.

Together with such chronological information, the composition of the produced magma accompanied by the lunar expansion is essential to understand the source property and related evolutional processes inside the Moon. The lunar surface holds maria of volcanic basalt, whose age peaks at 3.2–3.8 Ga and another peak around 2.0 Ga in the Procellarum KREEP Terrain (PKT) region (e.g., Hiesinger et al., 2003; Morota et al., 2011). The composition of lunar maria is known to vary with time. For example, the titanium content of the PKT maria increases by a few percent around 2.3 Ga (Kato et al., 2017; Sato et al., 2017). This transition indicates a change of magma source composition, possibly related to a hot plume containing IBC material. In addition to the present-exposed mare, several works have identified ancient basalt covered with highland regolith, the so-called cryptomare (e.g., Giguere et al., 2003; Whitten & Head, 2015a,b). Spectral comparison between cryptomare and lunar regolith samples has shown that low-titanium basalt matches ancient cryptomare basalts the most closely (Whitten & Head, 2015b). These combinations of temporal and compositional information on magmatism are essential to elucidate the lunar thermal history. However, no compositional constraints on magmatism directly related to the ancient expansion have been posed because magmatism during the global expansion is invisible in the surficial data solely.

In order to survey the geologic information related to the expansion, regions above lunar linear gravity anomalies (LGAs) are of particular interest. The NASA Gravity Recovery and Interior Laboratory (GRAIL) mission obtained high-resolution lunar gravity data (Zuber et al., 2013), enabling the identification of linear positive Bouguer anomalies with lengths of over-hundred kilometers (Andrews-Hanna et al., 2013). Based on their narrow and long geometries, LGAs have been interpreted as ancient vertical tabular intrusions or dikes denser than the surrounding crust. The random orientations of LGAs on both near- and farsides suggest that LGAs were formed under a globally-isotropic extension of the lithosphere (Andrews-Hanna et al., 2013). Furthermore, Sawada et al. (2016) have revealed that LGAs overlap topographic depressions like terrestrial great rift valleys, similarly indicating horizontal tensile stress during the LGA formation.

We emphasize that highland areas covering LGAs and superposing craters are the best locations to find evidence of ancient magmatism. Some LGAs are superposed by large craters, such as Rowland crater on LGA1 (Figure 1a and b), Roche crater on LGA2 (Figure 1c and d), Crisium basin on LGA4, and Edison crater on LGA20 (Figure 1e and f). Note that the LGA are numbered in the same way as Andrews-Hanna et al. (2013) and Sawada et al. (2016). Based on the previous estimation of LGA structures, the top depth of intrusions could be about 10 km in the shallowest case (Liang & Andrews-Hanna, 2022). Thus, these craters possibly excavated a

certain fraction of LGA materials. LGA material originally from a partially molten region in the mantle contains high-calcium pyroxenes (HCP) like lunar maria. This makes it impossible to identify excavated intrusions spectrally around Crisium basin, which is covered with mare basalts. On the other hand, spectra of highland regions are dominated by low-calcium pyroxenes (LCP), which have absorption features different from HCP (Cloutis & Gaffey, 1991; Denevi et al., 2007; Klima et al., 2007, 2011; Lucey et al., 2014; Ogawa et al., 2011; Yamamoto et al., 2015). Therefore, if highland craters (Rowland, Roche, and Edison) excavated LGA materials, distinguishable spectra of exposures might be found in the peripheries of those craters. Incorporating the chronological information of the craters and the cross-cutting relationships between these LGAs and craters, the age of the LGA formation could also be constrained by the presence of excavated materials.

To investigate the composition of ancient magmatism and the chronology of the initial lunar expansion, this paper analyzes the geology around Rowland, Roche, and Edison craters in terms of the LGA material and history. We first show the spectral features in the continuous ejecta region of these craters by finding candidates of basaltic exposures in a multiband reflectance map to see if they contain mare-like HCP and estimate the FeO and TiO_2 contents. Then, we investigate whether these exposures originated from the LGA material. Later in this paper, we simulate deformation and excavation during the cratering process to confirm the possibility of excavation in comparison with gravity data around LGA. Finally, we propose compositional properties of ancient magma sources and discuss the ancient lunar magmatic and thermal evolution.

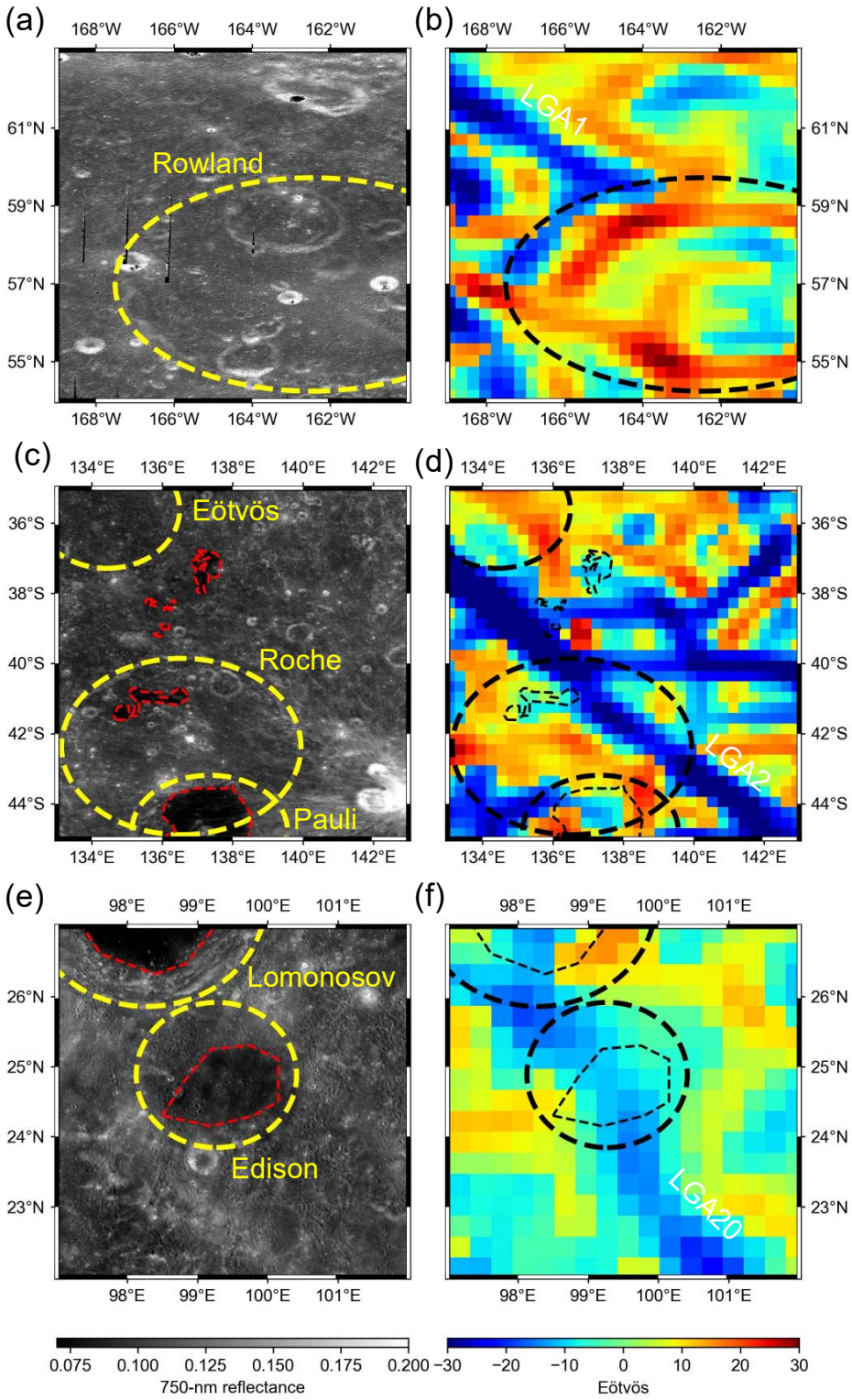

Figure 1. The Kaguya/MI 750-nm reflectance (a, c, e) and GRAIL gravity gradient maps (b, d, f) of regions analyzed in this paper. Crater rims are shown in the yellow and black lines on the reflectance and gravity gradient maps, respectively. Small maria are shown as the red and black lines on the reflectance and gravity gradient maps, respectively. The LGAs are traced with white

133 dashed lines on the gravity gradient maps. (a, b) Rowland crater and LGA1. LGA1 seems to
134 terminate around the rim of Rowland crater. (c, d) Roche crater and LGA2. LGA2 penetrates
135 throughout Roche crater. This region possesses small maria (Pasckert et al., 2015a). (e, f) Edison
136 crater and LGA20. LGA20 seems to cross Edison crater.

137

2 Spectral analysis method

To identify probable ancient magma exposures, we analyzed spectral datasets obtained by previous lunar missions, following two steps. First, we made a compositional map within the targeted area by using the Multiband Imager (MI) data (Ohtake et al., 2008) taken by the Japanese lunar orbiter Kaguya. MI has the advantage of mapping the material distribution with a high spatial resolution, but it is still difficult to distinguish between LCP and HCP from MI whose spectral resolution is not sufficient to determine 1000- and 2000-nm absorption centers of pyroxenes. Therefore, we complementally analyzed hyperspectral data from the Moon Mineralogy Mapper (M^3) onboard the Chandrayaan-1 spacecraft.

2.1 MI map data analysis

Our analysis used MI_MAP products that include mosaics of reflectance at nine bands from visible to near-infrared wavelengths. The MI camera is equipped with five visible (415, 750, 900, 950, and 1000 nm) and four near-infrared (1000, 1050, 1250, and 1550 nm) bands. The published MI_MAP products have already been normalized by a photometric function with local topography, corrected via a reflectance comparison between the Apollo-16 sampling site and a lunar soil sample (Ohtake et al., 2008, 2013; Yokota et al., 2011). The spatial resolution of MI_MAP is 2048 pixels/degree, corresponding to 15 m at the equator. However, accuracy of image registration is not so high that we binned the data by 4×4 pixels to reduce the error. Also, some values are unreasonably lower than zero because of shadows in steep areas such as crater walls. Thus, we neglected such pixels for this binning process and in the latter analysis.

Searching for fresh basaltic materials, we made an RGB color composite map of spectral absorption depths (M. Ohtake et al., 2014; Taguchi et al., 2017) (**Figure 2**a). First, we normalized the spectrum by a continuum between 750 and 1550 nm at each binned pixel and mapped the absorption depths from the continuum at 950, 1050, and 1250 nm. Then, we composited these three maps as RGB (red: 950 nm; green: 1050 nm; blue: 1250 nm). Olivine and pyroxene that comprise lunar basalts exhibit spectral depressions at these bands, so basaltic materials are shown in whiter colors. On the contrary, anorthosite exposure appears blue due to a lack of absorption at the 950- and 1050-nm bands. In addition, space weathering on the Moon generally weakens the absorption features of minerals, so fresh materials are brighter on the map.

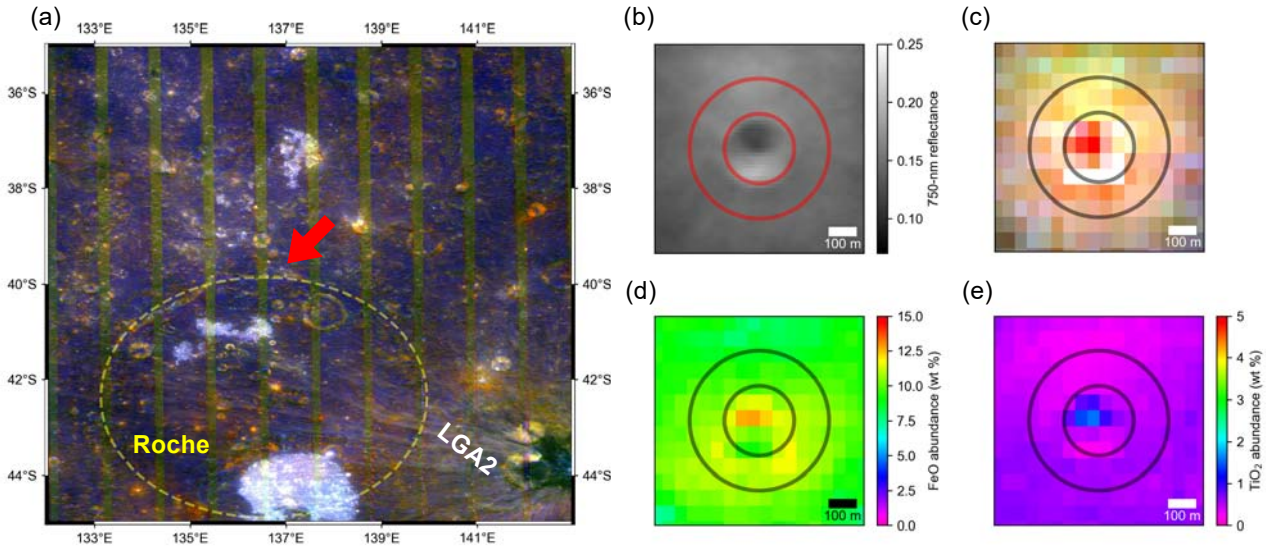

Figure 2. (a) RGB composite map around LGA2. (b-e) Maps of 750-nm reflectance, RGB composite, FeO abundance, and TiO_2 abundance at P1 (indicated by the red arrow in (a)). The red or black lines show circles with one and two radii of the fresh crater whose inside is filled with basaltic material. Note that the images except for (b) are binned by 4×4 pixels.

We next selected candidates of basaltic exposures from the composite map by visual inspections and categorized them morphologically (**Figure 2**b). Comparing topography from SLDEM2015 (Barker et al., 2016) with 750-nm reflectance maps, we carefully chose spots whose colors are white on the map (**Figure 2**c). The fresh material is generally exposed around new craters or at steep slopes, so we attached flags, such as "crater" or "slope", to the selected places, depending on their morphologies. It should be noted that white spots in topographically low areas are excluded because these sites are perhaps small maria. As endmember spectra for the latter analysis, we also extracted data in both highland and mare that particularly exhibit high Optical Maturity Parameter (OMAT) values and, therefore, are fresh (Lucey et al., 2000).

Finally, we characterized compositions around the candidates. From empirical algorithms deriving iron and titanium contents from MI reflectance ratios (Lucey et al., 2000; Otake et al., 2012), FeO and TiO_2 distribution were calculated. We then estimated their average and standard deviation for each location. At exposures on slopes, we manually fitted a circle on white pixels and simply averaged values. In the case of craters, we averaged values outside a circle fitted to the crater rim, as shown in **Figure 2**d and e. Depending on the illumination conditions, reflectance values occasionally become unrealistic within craters, making iron and titanium contents too high or low. To avoid significant errors due to these problems, we calculate the azimuthal average and standard deviation of area 1–2 crater radii away from its center. This region is covered by continuous ejecta (Melosh, 1989; Moore et al., 1974), allowing us to treat it as a representative value of materials exposed by the fresh crater.

2.2 M^3 data analysis

We analyzed hyperspectral reflectance around the candidates using the M^3 L2 products. M^3 was an imaging spectrometer that obtained cube images composed of two spatial and one

spectral dimensions. M^3 covered wavelengths approximately from 400 to 3000 nm with spatial resolutions of 70–140 and 140–280 m/pixel for Target and Global modes, depending on the spacecraft altitude (Green et al., 2011; Pieters et al., 2009). The reflectance data have been published as the L2 products after solar irradiance correction, statistical polishing, removal of thermal emission, and photometric correction (Besse et al., 2013; Boardman et al., 2011; Clark et al., 2011; Green et al., 2011; Isaacson et al., 2013). It should be noted that the ground truth correction is not applied to the L2 product, but the correction factor derived from the average 62231 soil is also published in the M^3 data archive. It is well known that this correction improves the characterization of the 1000-nm absorption position on highland soil. The correction factor varies depending on M^3 optical periods because a wide range of the detector temperature due to the solar zenith angle generates artifacts in the acquired spectra (Isaacson et al., 2013). Therefore, we applied the correction factors of corresponding optical periods to each L2 product in the latter analysis.

As a preprocess prior to the determination of pyroxene type at each location, a continuum was subtracted from the corrected reflectance in the same manner as Whitten & Head (2015b). Due to space weathering, lunar spectra have a red-sloped continuum, which disturbs the analysis of accurate mineralogical absorption and has been removed in previous lunar hyperspectral characterization (e.g., Isaacson et al., 2011; Sunshine et al., 1990; Yamamoto et al., 2018; Yamamoto & Watanabe, 2021). For this continuum removal, our analysis employed the convex hull method that finds a polygonal line connecting three tie points (Figure 3a). The first tie point was set at 750 nm, but the second and third were able to vary in the wavelength range of 1329–1778 nm and over 2776 nm, respectively. The second and third tie points were selected so that the polygonal line among the three tie points did not intersect with the M^3 spectrum. Finally, the spectrum was divided by this two-parted linear continuum, and the band depth at each wavelength was calculated.

To identify the pyroxene type, the modified Gaussian model (MGM) was then applied to the continuum-removed spectra. MGM has been known as a robust algorithm to characterize pyroxene spectra in visible to near-infrared wavelengths (e.g., Denevi et al., 2007; Sunshine et al., 1990), in which the spectra can be deconvoluted to several Gaussians. The central wavelengths of deconvoluted Gaussians are significant indicators of pyroxene compositions. Based on previous reflectance analysis on natural and synthetic pyroxenes (Denevi et al., 2007; Klima et al., 2007, 2011), Gaussians centered at 900–1000 and 1800–2400 nm have their peaks at shorter wavelengths for LCP and vice versa for HCP. Additionally, HCP has an absorption at 1300 nm, although LCP exhibits no absorption there. Therefore, our analysis fitted four Gaussians to the spectra by setting the initial centers of Gaussians at 300, 1000, 1300, and 2000 nm in the same manner as Ogawa et al. (2011). The calculated band positions were finally compared with those of synthetic and natural LCP and HCP (Denevi et al., 2007; Klima et al., 2007, 2011). In order to avoid noisy spectral data in the latter discussion, exposures only with a maximum absorption depth at 900–1000 nm larger than 10 % and root-mean-square of fitting residual less than 0.02 are chosen. This limitation on the signal-to-noise ratio in our M^3 analysis, therefore, reduced the number of analyzed exposures from that in the MI data analysis.

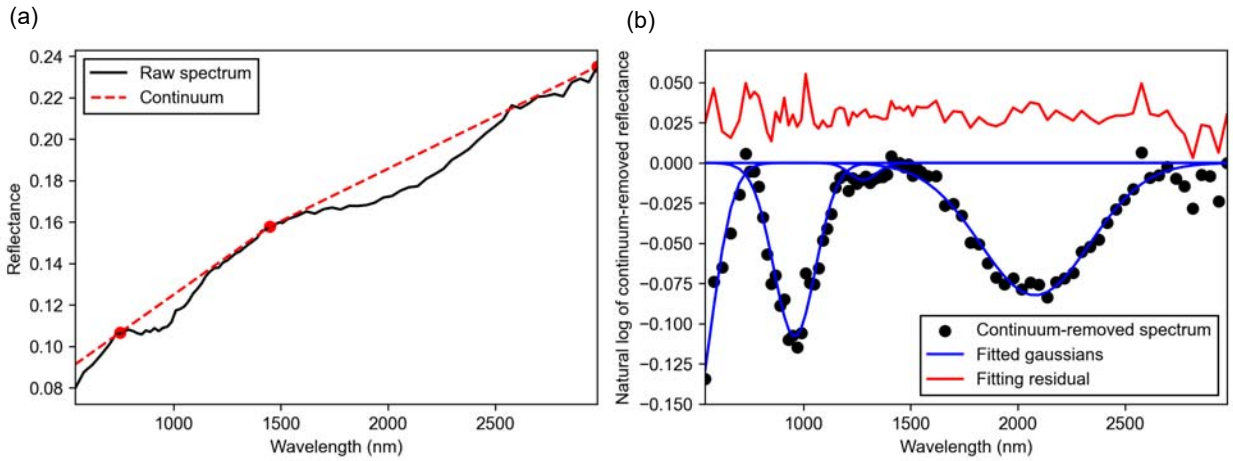

Figure 3. Example of spectral analysis routine for M^3 dataset. (a) One of the spectra at LGA2-E1 from the image of M3G20090529T060422. The spectrum after all the calibration is shown in black. The red points correspond to tie points used for a two-parted linear continuum generation shown as the red dashed line. (b) Demonstration of our MGM deconvolution. The black dots are the natural log of reflectance values normalized by the continuum. The blue lines are four Gaussians fitted to the continuum-removed reflectance. The fitting residual is shown in red with an offset of 0.03.

3 Spectral features around LGAs

3.1 LGA1

Around Rowland crater, the number of locations with white colors is much less than LGA2 (Figure S1). We totally selected 13 pyroxene-rich exposure candidates inside and outside Rowland crater and labeled them with a mark of exposure (E) and ID number. Note that the spots inside Rowland were included in the analysis, too, because magmatic material could be mixed within the crater during its formation. For comparison, we also extracted 8 anorthositic spots on the composite map as typical highland materials. It should be noted that no maria exists in this region (Figure 1a). The longitude and latitude of each location are summarized in Table S1.

The MI data around LGA1 revealed almost no signs of significantly high FeO and TiO_2 abundances. The MI data of this region commonly exhibits FeO and TiO_2 abundances lower than 4 wt.% and 1 wt.%, respectively (Figure S3 and S4). FeO and TiO_2 abundances at the exposures show the same tendency as other areas in Figure 4a. Except for a few candidates, such as E3, FeO abundance in these exposures is less than half of that in typical maria (Figure 4c and e). These values are within the range of noritic materials (Lucey et al., 1998), which is thought to be a typical rock type of the lunar lower crust.

The M^3 spectral features indicate that the pyroxene characteristic in this region is similar to LCP. Figure 4b shows a comparison of the absorption peak positions at 1000- and 2000-nm bands to laboratory LCP data. Owing to the low signal-to-noise ratio and weak absorption in the M^3 data of this region, the number of candidates was limited. However, the calculated 2000-nm peak positions were always shorter than 2100 nm, ranging similarly to the synthetic LCP data. LCP is known to be dominant on the spectra of noritic rocks. Therefore, these pyroxene

exposures around LGA1 can be interpreted as materials ejected from the noritic lower crust, not from basaltic magma intrusions composed of HCP.

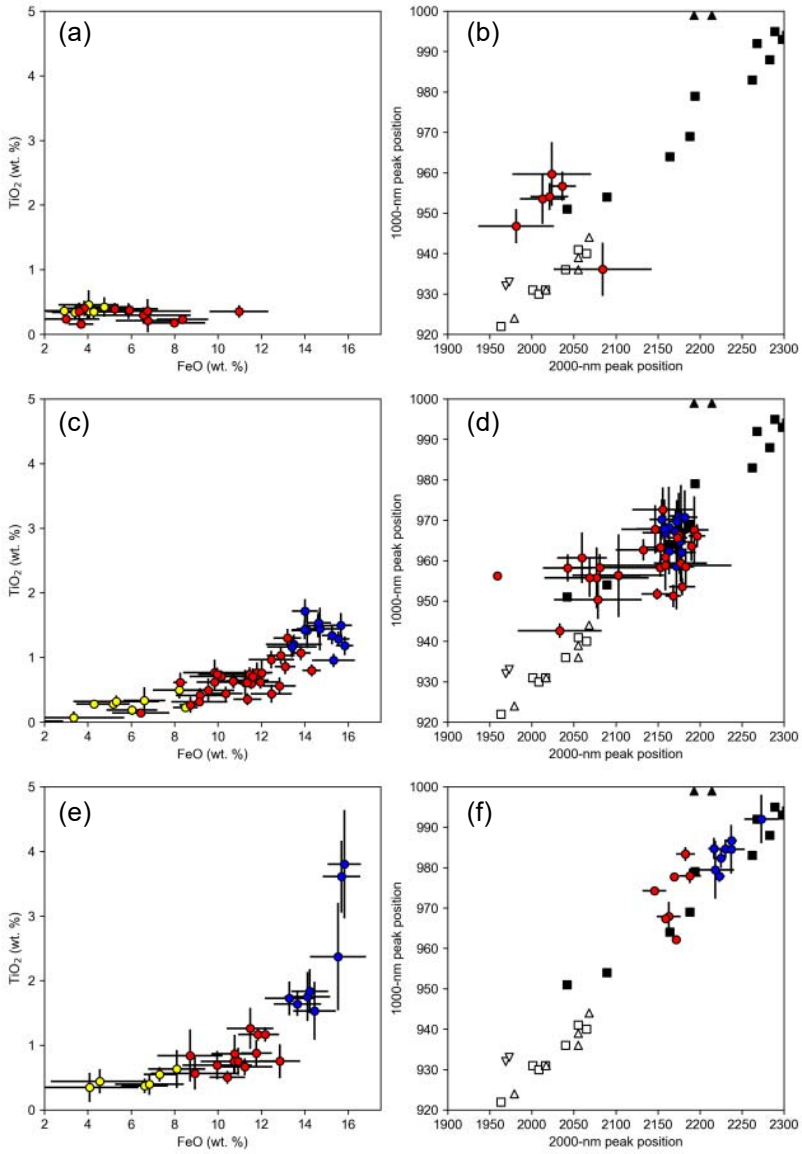

Figure 4. Compositional summary of the spectral analysis results. FeO and TiO_2 abundance at exposure candidates. The blue and red points correspond to pyroxene exposures on the highland and maria labeled with E and M, respectively. The yellow points are highland crust exposures with bluer colors on the composite map. (a, c, e) FeO and TiO_2 abundance at each location. The error bar is a standard deviation of the value within the extracted area. (b, d, f) 1000- and 2000-nm absorption peak positions at exposure candidates. The error bar is a standard deviation of the M^3 pixels of those candidates. The black square and triangles are synthetic clinopyroxene (HCP) data from Denevi et al. (2007) and Klima et al. (2011), respectively. The white squares and triangles are synthetic and natural orthopyroxene (LCP) data from Denevi et al. (2007) and Klima et al. (2007), respectively. Results are summarized for each region: (a, b) around LGA1, (c, d) around LGA2, and (e, f) around LGA20.

3.2 LGA2

From the MI composite map around LGA2, we found 31 white exposures in the northern area of Roche crater. Because Roche crater is superposed by Pauli crater, the southern part of this area is excluded conservatively in this study (Figure 1). The eastern side of Roche is not analyzed, either, due to contamination by bright ejecta rays from the Eratosthenian-aged Ryder crater.

It is noteworthy that this region contains small maria between Eötvös and Roche craters (Figure 1). Pasckert et al. (2015) and Wilhelms & El-Baz (1977) have already identified young mare parches inside Roche and Pauli craters. Our comparison between the composite and topography map reveals four additional candidates of mare patches in the northern part of Roche (Figure S5). The composite color of these candidates appears white in a topographically low area, indicating basaltic materials confined in topographic depression. They were considered as basalts that erupted in the same way as nearby maria, and hence we carefully excluded these areas from our exposure identification. These locations were included as mare exposures (marked with M and ID number) and compared to other pyroxene exposures later.

The FeO contents of the pyroxene exposures are probably a mixture of mare and highland materials. As shown in Figure 4c, the candidates are distributed continuously between highland and mare materials. Some of their FeO contents exceed even 12 wt.% and are higher than noritic lunar rocks (Lucey et al., 1998). However, the values are slightly lower than that of maria. Similarly, their TiO_2 contents range from 0.5 to 1.3 wt. %, varying between mare and highland materials. Thus, the compositional characteristic of these pyroxene-like exposures indicates a mixture of highland anorthosite and mare-like basaltic material.

The absorption peaks additionally support a mixture of basaltic material within the anorthositic crust around LGA2. In Figure 4d, the majority of both 1000- and 2000-nm peak positions are distributed out of LCP but in a range similar to HCP. While both 1000- and 2000-nm peak wavelengths are shorter than those of the majority of synthetic clinopyroxene and some of them are similar to LCP, the majority of their distribution is laid within the same range as maria. Furthermore, many of them possess almost the same peak positions as the maria in this region, indicating a mixture of basaltic material as the FeO and TiO_2 trends show.

3.3 LGA20

LGA20 possesses brighter exposures, particularly in the southern area of its center, in the composite map, and we found 13 candidates in total. The areas inside Edison and Lomonosov craters are covered by maria (Figure 1), so we selected 8 fresh craters on the mare region as the reference of basalt.

The FeO and TiO_2 contents are distributed between mare and highland materials continuously in the same manner as LGA2. As shown in Figure S3, the FeO content around LGA20 ranges from 8 to 10 wt % on average, which is much higher than that of the typical highland. Some of the locations near the rim of Edison crater exhibit FeO of 10 % or even higher. The variation of TiO_2 content is also similar to that around LGA2 and stays in the range

of 0.5 – 1.5 wt%. On the other hand, the TiO_2 content in the mare region is more widespread than that around LGA2 because the mare inside Lomonosov crater has more abundant TiO_2 (see Figure S4), possibly because of a temporal change of magma compositions in this region or contamination of Edison's mare by low-FeO highland material (Giguere et al., 2003).

The 1000- and 2000-nm pyroxene absorption peaks also manifest the existence of HCP around Edison crater. The discovered pyroxene exposures have absorption peaks in the range of clinopyroxene (Figure 4). The main difference from LGA2 is that the peak wavelengths are a little shorter than those of mare. This could be due to a different extent of contamination by numerous ejecta or a compositional difference between maria and pyroxene exposures. Roche and Edison craters are Nectarian and Pre-Nectarian aged, respectively, and the excavation event by Roche crater predates that by Edison. Thus, a mixture of highland material is more enhanced around LGA20 than LGA2.

3.4 Possible sources of discovered basaltic exposures

Our spectral analysis found that the peripheries of LGA 2 and 20 possess abundant exposures with high FeO and HCP-like adsorptions. These basaltic spectra and compositions suggest ancient excavation of basaltic LGA materials by Roche and Edison craters. However, this discovery might also be attributed to other causes: ejecta from a mare, impact melt, pyroclastic material, and mafic melt trapped within the crust during the magma ocean solidification.

The first possibility of basaltic ejecta from mare regions is excluded by ejecta distribution modeling. The regions where basaltic exposures are discovered contain some small maria that also have HCP and high FeO abundance. One of the end members of the material mixture indicated by our spectral analysis could be the deposition of basaltic mare material ejected from craters on small maria after the Roche/Edison formation. To estimate this effect, we integrate the empirical relationship between ejecta thickness and distance from a crater (McGetchin et al., 1973; Melosh, 1989) with one of the most detailed lists of craters with a diameter of 1 km or larger (Wang et al., 2021). Figure 5 shows the ratio of ejecta from mare regions (red lines in Figure 1c and e). As obviously shown, the ejecta deposited on the pyroxene candidates is dominated by highland ejecta, and the ratio of ejecta from mare craters is always lower than 20 wt. %. Such a low mixing ratio makes the FeO contents as low as highland material, inconsistent with the observed values. Therefore, the observed HCP exposures cannot be explained by ejecta from basaltic surface units.

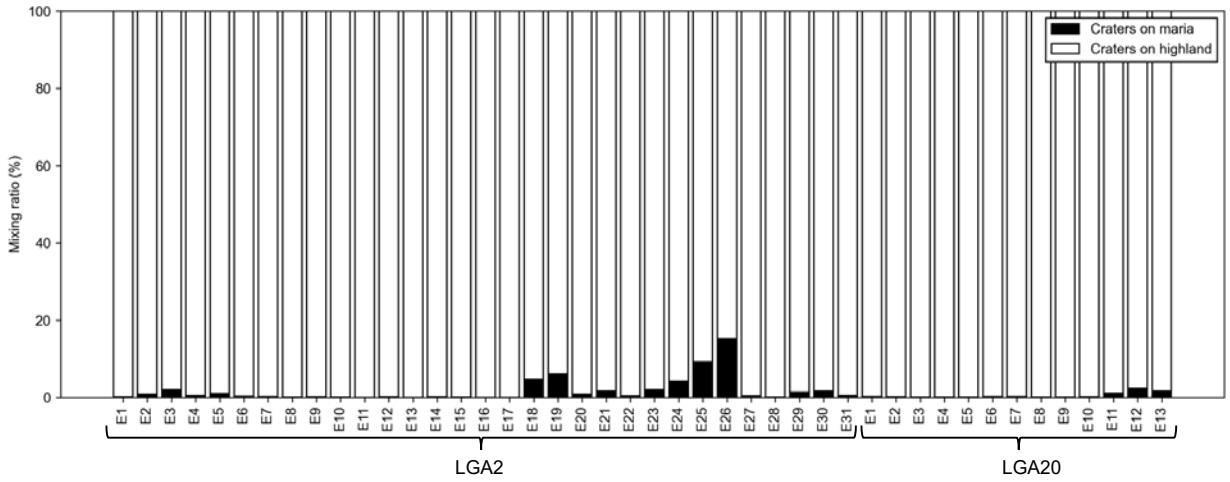

Figure 5. The ratio of ejecta deposited at each HCP exposure around LGA2 and 20. The black and white boxes show the contribution of ejecta from craters on mare and highland, respectively.

The impact melt is also unlikely for the source of these exposures. Once a crater-forming impact occurs, this energetic event melts the target material. Previous remote-sensing data of impact melt show absorption peaks consistent with HCP (e.g., Moriarty & Pieters, 2018). However, topography around the pyroxene exposures is not consistent with impact melt. While impact melt often forms pond-like morphology, topographic depression is excluded from the exposure candidates as described above. Also, areas nearby the candidates do not have morphology specific to impact melt, like flow features and cooling fractures, as seen in impact melt around other craters (e.g., Krüger et al., 2016). Moreover, the mass fraction of melt product in ejecta would be less than 10 wt % based on the empirical formula for gabbroic anorthosite (Melosh, 1989) and numerical simulations (Liu et al., 2022), which is inconsistent with the observed FeO content.

In addition, the observed spectra reject the possibility that the exposures originated from pyroclastic deposits. Similar to dark mantle deposits identified on the Moon (e.g., Besse et al., 2014), this high-FeO material could be composed of pyroclastic glasses emplaced by explosive volcanic eruptions. By using Clementine multispectral images, Giguere et al. (2003) categorize the southern region of Edison crater as dark mantle deposits of probably pyroclastic origin based on its low albedo. Such pyroclastic material could appear to have moderately high FeO abundances via our estimation from multiband reflectance. This is because the empirical formula between reflectance and FeO is not calibrated for glasses, possibly enhancing the FeO abundance at dark mantle deposits unreasonably. However, the peak positions of dark mantle deposits in the 1000- and 2000-nm bands range above 990 nm beyond 2000 nm (e.g., Besse et al., 2014; Kumaresan & Saravanavel, 2022). These ranges are outside the continuous distribution of pyroxenes in Figure 4.

The final alternative source is mafic melt trapped within the crust, but this seems unlikely as well. Several studies on lunar hyperspectral data have identified HCP mixture in highland craters, which perhaps suggests the existence of mafic liquid trapped within the anorthositic cumulates during the lunar magma ocean solidification (Ogawa et al., 2011; Yamamoto et al., 2015). Numerical simulation by Piskorz & Stevenson (2014) also suggests that mafic melt

cannot wholly be expulsed from the lunar crust shallower than 5 km during the formation of floating anorthosite cumulates. On the other hand, a global survey of HCP by Yamamoto et al. (2015) shows that no craters with diameters less than 6-10 km possess HCP. Their result implies that the uppermost crustal layer within a depth of 1 km is dominated by LCP rather than HCP. To exclude this possibility, our analysis focused on craters with diameters of 8 km at maximum, and the majority of them are smaller than a few hundred meters.

In summary, the pyroxene exposures analyzed in our study are the most likely to originate from basaltic material, which does not exist on the present lunar surface as either maria or impact melt. In particular, all the hypotheses above fail to explain the difference in the existence of HCP exposures between Rowland and Roche craters, and another hypothesis to bring basaltic material to the region is necessary.

4 LGA excavation indicated by gravity anomaly

A possible source that could be attributed to the spectral difference among Rowland, Roche, and Edison craters is the subsurface LGA material excavated by the analyzed craters. To investigate if these HCP exposures came from the subsurface ancient dikes or not, we next compare cratering simulation results and lunar gravity data. Interestingly as seen in Figure 1, the linear structures in the lunar gravity gradient map have different characteristics inside craters; LGA1 appears terminated at the rim of Rowland crater, but LGA2 penetrates through the Roche crater. Both craters have similar diameters of around 160 km. Therefore, we simulate the subsurface modification and excavation by these craters and calculate variations of gravity anomalies after the crater formations to test the LGA excavation hypothesis.

Our gravity modeling consists of two parts; (i) estimation of possible subsurface structures from the GRAIL gravity data and (ii) simulation of gravity change due to excavation and deformation of the subsurface structure by the crater formations. Due to the non-uniqueness of gravity inversion, a certain variety of subsurface structures satisfies the observed gravity data. Thus, we first prepare a set of intrusion shapes from gravity data outside the featured crater where crustal deformation due to impact is assumed to be negligible. Various density differences between the intrusion and surrounding crust are taken. Next, we simulate the subsurface modification for every pattern of the shape with the iSALE shock physics code (Amsden et al., 1980; Collins, 2014; Collins et al., 2011; Collins et al., 2004; Ivanov et al., 1997; Melosh et al., 1992; Wünnemann et al., 2006) and gravity structure above the crater interior after its formation. Finally, we compare the simulation and observed data, and discuss the cross-cutting relationship between LGAs and the craters.

4.1 Modeling procedure

We begin with preprocessing of Bouguer gravity data around the craters by filtering specific wavelengths and rotating the coordinates. In the same manner as Andrews-Hanna et al. (2013), we first make a band-passed Bouguer anomaly map. From a lunar Bouguer-corrected gravity model of GRGM1200A_BOUGUER (Lemoine et al., 2014), we extract the spherical harmonics coefficients with degrees of 50-300 to filter out the noise effect and long-wavelength

structures. The filtered gravity map was next rotated using spherical harmonic transformations so that LGA is located on the lunar equator. This allows us to apply a Cartesian coordinate in our latter analysis because the scale of interest is much smaller than the radius of curvature of the Moon (Liang & Andrews-Hanna, 2022).

The possible patterns of LGA structures before cratering are estimated by fitting a rectangular density anomaly to the gravity data outside the crater, assuming that the subsurface structures of LGA continue both outside and inside the crater before its formation. We regard the average of LGA values outside the crater as typical pre-cratering gravity. It should be noted here that the gravity profile perpendicular to LGA was averaged by aligning peak gravity horizontally because LGA is not completely linear. Then, we fit gravity values from an intrusive subsurface body with a uniform density to the averaged LGA profile. The density of magma intrusion is as high as that of the mare basalt (Kiefer et al., 2012), but the source of gravity could be a swarm of dikes, which reduces the density difference rather than a single giant dike (Andrews-Hanna et al., 2013). Thus, the density difference between the intrusion and crust varies from 200 to 1000 kg/m^3. Owing to the non-uniqueness of the gravity inversion, the shape of the intrusive body has to be assumed in addition. In principle, the LGA value can be fitted by other complex shapes, such as T-like prisms, but Liang & Andrews-Hanna (2022) has revealed that changing the assumed shape does not significantly improve the fitting. Therefore, we assume the simplest tabular intrusion hereafter, as Andrews-Hanna et al. (2013). A Bayesian approach by Andrews-Hanna et al. (2013) indicated that the probability of a top depth of less than 5 km is not zero. On the other hand, no mafic spectrum is observed just above the LGA, meaning that LGA material does not reach the surface directly. Thus, we set a non-zero top depth at every 2 km interval. Then, with the assumed density and top depth of a tabular intrusion, its width and center position are treated as fitting parameters (Figure 6). It should be noted that the root of the intrusion is placed at the Moho boundary. Because magma is negatively buoyant everywhere above the lunar Moho, it is difficult to stall the dike without any pressure from magma in the mantle (Wilson & Head, 2017).

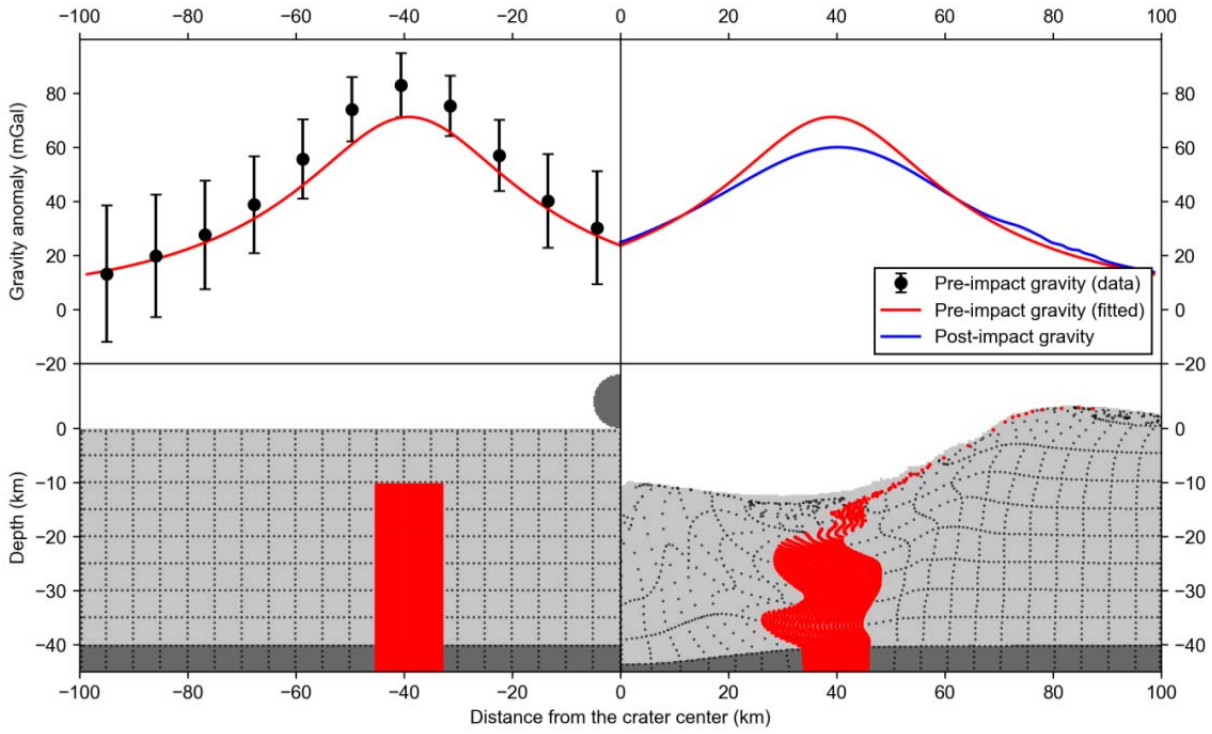

Figure 6. An example of our LGA modification simulation. The left and right figures show the result before and after cratering, respectively. The upper and bottom figures show the gravity profile perpendicular to LGA and the subsurface material distribution, respectively. The origin of the x-axis corresponds to the crater center. In the top-left figure, the gravity anomaly from a rectangular body (red line) is fitted to the averaged gravity profile (black points). In the bottom left figure, the corresponding rectangular intrusion is shown in red. The light and dark pixels are the crust and mantle. The dark semicircle in the bottom-left figure is the projectile. The blue line in the top right figure shows the gravity profile from the modified intrusion. The density difference and top depth assumed in this figure are 400 kg/m^3 and 10 km, respectively.

The subsurface material movements by a meteoroid collision were numerically traced by a crater-forming simulation. In this work, we use the iSALE-2D shock physics code (Amsden et al., 1980; Wünnemann et al., 2006), which is based on the SALE hydrocode solution algorithm (Amsden et al., 1980). To simulate hypervelocity impact processes in solid materials, SALE was modified to include an elastoplastic constitutive model, fragmentation models, various equations of state (EoS), and multiple materials (Ivanov et al., 1997; Melosh et al., 1992). More recent improvements include a modified strength model (Collins et al., 2004), a porosity compaction model (Collins et al., 2011; Wünnemann et al., 2006), and a dilatancy model (Collins, 2014). In our simulation, a dunite projectile with a radius of 5 km collided on the lunar surface at the speed of 20.9 km/s. This impact speed was the same as the median speed of an asteroid collision with the Moon during the Late Heavy Bombardment epoch (Bottke et al., 2012). The target was assumed to be a two-layered surface composed of basalt crust and dunite mantle. As a result, a crater with a diameter of 160 km was formed in our simulation. All the parameters are

summarized in Table S2. In addition, it should be noted here that the choice of materials does not make a substantial difference, as reported by (Melosh et al., 2013; Miljković et al., 2015).

The gravity before and after the collision was calculated by integrating the iSALE tracers, which are originally located within the fitted tabular body. The positions of tracers are moved by cratering within a vertical plane that contains the original tracer location and crater center. Because our cratering simulation is axisymmetric, we calculate a cross-section of the LGA body at each azimuth and integrate them to determine the positions of tracers in cylindrical coordinates. Each tracer is treated as a rectangular box with the assumed density, and its gravity anomalies were summed up to make a gravity map after the crater formation. In particular, the gravity value within a distance of 15 km from the intrusion center changed after crater formation and was reduced by 30 mGal at most, as demonstrated in Figure 6. Thus, we focused on the gravity within this narrow region inside the crater. Note that our simulation treats a homogeneous crust because calculation only with the iSALE tracers is sufficient to estimate gravity change due to the subsurface modification. Although the density gap between the LGA intrusion and surrounding crust causes the reflection of shock waves and could suppress the modification beneath the crust, we confirmed that such a density gap little affects the overview at all. Even if the density gap is set over 800 kg/m^3, the difference in resultant gravity between homogeneous and heterogeneous crust models is less than 5 mGal (Figure S6).

Another contribution to the gravity inside craters comes from porosity change during the crater formation. Soderblom et al. (2015) show that the Bouguer anomaly of lunar complex craters has a negative value on average, implying that the porosity beneath the crater is higher than the crust due to the fracturing by shock waves. Their analysis also reveals that the average gravity inside the crater has a significant variation among craters, ranging from +10 to -40 mGal. These wide-spreading values originate from the pre-impact porosity beneath the crater because the impact can also close pores inside highly fractured material (Milbury et al., 2015). In addition, the gravity anomaly could be variable inside the crater. For example, if the initial porosity is high, pore closure is enhanced more in the central region of the crater than the outer area, resulting in a high Bouguer anomaly around the crater center. This could affect the gravity profile in our analysis, especially in the case of LGA1, whose direction is nearly toward the center of Rowland crater. To include these pore creation and destruction in our simulation, we include the dilatancy model to consider a variety of the initial porosity effect, following the parameters presented by Collins (2014), Milbury et al. (2015), and Miljković et al. (2021) (Table S2). The LGA gravity inside the crater is weaker than that outside for both Rowland and Roche craters, suggesting that the initial porosity was low. Milbury et al. (2015) have already shown that an initial porosity of 6.8 % generates positive gravity values inside a 160-km-sized crater. Thus, we set the initial porosity for various values from 0 to 8 %. Next, we add the various gravity profile from dilatancy to that from the LGA modification. After binning the simulated gravity distribution to the same resolution as the data, we then find the best-fit dilatancy model to minimize the residuals of our simulation from the data. For this comparison, we use pixels that are located inside the crater and within 10 km of the LGA center, corresponding to the area where the gravity is affected by both impact processes. Finally, we take the gravity signature with the best-fit dilatancy as the best-gravity model for each case of assumed parameters.

4.2 Rowland crater on LGA1

518 Our numerical simulation reveals that LGA1 has not penetrated Rowland crater. The
519 simulated gravity profile was never consistent with the observed one inside the Rowland crater,
520 especially the substantial gravity gap between the rim and center. The gravity anomaly and
521 gradient data show that the gravity inside Rowland crater drops for more than 70 mGal adjacent
522 to the apparent LGA1 (Figure 7c) and appears terminated at the crater rim in the gravity gradient
523 map (Figure 1b). This gravity drop is much larger than that by the excavation and deformation in
524 the crater formation. Figure 7b shows the case that the density difference, top depth, and initial
525 crustal porosity are assumed to be 400 kg/m^3, 10 km, and 2.0 % respectively. Figure 7c
526 demonstrates that the gravity value after the collision decreases inside the crater. The Bouguer
527 anomalies within the area surrounded by two black dashed lines in Figure 7a and b are averaged
528 along the y-axis (the black, red, blue, and green lines in Figure 7c). The simulated value goes up
529 and down qualitatively in the same manner as the observed data. However, the LGA-like gravity
530 still appears to continue throughout the Rowland crater because the gravity drop nearby the rim
531 is only about 30 mGal and a factor of two less than the observed drop (Figure 7b).

532 The discrepancy between our numerical simulation and the observed gravity anomalies is
533 caused by a remaining root of the intrusion. To account for the high gravity at the central part of
534 Rowland simultaneously, the best-fit dilatancy model makes the gravity drop of only 15 mGal
535 nearby the rim as shown by the green line in Figure 7c. On the other hand, the LGA modification
536 decreases the Bouguer gravity by only 15 mGal in the crater for this case. As demonstrated in
537 Figure 6, the crater formation is not able to destroy all the structures of the intrusion. Therefore,
538 the root of the intrusion still remains beneath the simulated crater, failing to explain the complete
539 termination of LGA at Rowland's rim in the observed data.

540 Any simulated gravity profiles cannot describe the specific gravity signature inside the
541 Rowland crater, implying that LGA1 did not pre-exist before the Rowland formation. To make
542 sure of this finding, we investigate all the sets of assumed density and top depth. We calculated
543 differences in the average gravity profiles between observation and simulation (black and blue
544 lines in Figure 7c). The gravity just above the LGA location is non-uniform, which would be an
545 original variation of LGA before the crater formation. Thus, the difference was normalized by a
546 standard deviation of LGA gravity (black error bar in Figure 7c). To examine the similarity
547 between the gravity value and profile shape quantitatively, we focus on the normalized
548 difference at the local gravity minimum and maximum inside the crater. In Figure 7d, the
549 normalized differences between the observation and simulation are shown for all the assumed
550 parameter sets. Although the local maximum can be reproduced within two standard deviation
551 ranges with a couple of parameter sets, the difference at the local minimum is always larger than
552 three standard deviations. This implies that the great gravity gap next to the terminator of LGA
553 cannot be attributed to the cratering excavation and is evidence that LGA1 did not continue
554 beyond the Rowland rim even before the crater formation.

555

556

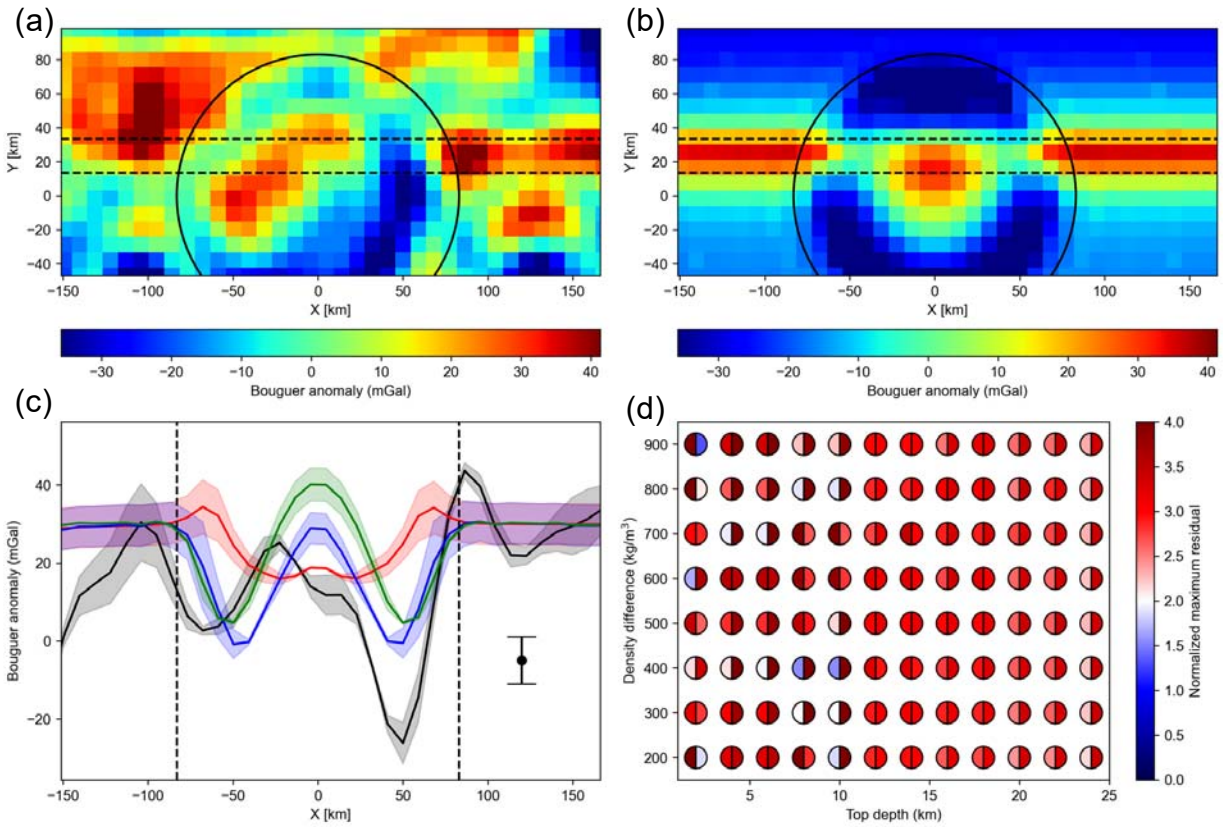

Figure 7. Comparison between simulations and the observed data. (a) The Bouguer anomaly map around Rowland crater. The solid black line shows the rim position. The area between the two black dashed lines is the area used for the comparison. Note that the coordinate is rotated to make the LGA direction parallel to the x-axis. (b) An example of a simulated Bouguer anomaly map when the density difference, top depth, and initial crustal porosity are assumed to be 400 kg/m^3, 10 km, and 2.5 %, respectively. (c) The averaged gravity profile within the compared area. The observed data is shown in the black line. The red, green, and blue lines show the gravity change by the LGA modification, porosity change, and the sum of these two effects. The shaded areas correspond to a standard deviation range within the compared area along the y-axis. The black error bar shows a standard deviation of the LGA gravity outside the crater. (d) The normalized difference at the local maximum and minimum within the crater. The colors in the right and left semi-circles show the values at the local minimum and maximum, respectively.

4.3 Roche crater on LGA2

On the contrary, our simulation successfully reproduces gravity signatures similar to the LGA2 values inside the Roche crater. As shown in Figure 1d and 8a, the gravity inside the Roche is weaker than that outside but a linear feature extends across the Roche crater. This feature is also seen in our numerical simulation. Figure 8b and c demonstrate an example case simulated under the same assumption of the density difference and top depth as Figure 7. The excavation and deformation of LGA blur the linear feature, but the remaining root of LGA

beneath the excavation depth of Roche still appears as a continuation of LGA. The average gravity decrease of about 50 mGal inside Roche crater is not as extreme as that inside Rowland crater. As shown in Figure 8c, this moderate decrease can be attributed to the sum of the LGA modification and porosity production due to the Roche formation. This comparison between simulated and observed gravity implies that LGA2 was affected but not entirely destroyed by the crater formation.

The comparison between the simulation and data for all the parameter sets confirms the effect of the impact cratering on LGA2. Figure 8c shows that the averaged gravity within Roche crater floor has a variation with a range of 20 mGal. Because the LGA2 gravity outside Roche crater also has a variation, we investigate whether the simulated profile matches the data at the local maximum and minimum in the same way as LGA1. Figure 8c depicts that the gravity signature always agrees with the observation within 1.5 standard deviations. Thus, the porosity and intrusion modification well explains the LGA2 gravity decrease inside Roche crater.

Figure 8d also implies that the favorable top depth of the intrusion is shallower than 22 km. As Figure 8c demonstrates, the intrusion body at the deep area is modified but still remains in almost the same position. The gravity decrease by the LGA modification is hence less than 5 mGal if the whole intrusion exists deeper than 22 km before the impact. In addition, the gravity decrease is limited to the locations nearest to the crater center (Figure 8c), where the depth of the excavated and modified region is the deepest on LGA2. This value is too small to explain the observed gravity decrease of 50 mGal even with negative gravity from porosity production because the observed gravity decreases inside lunar craters with a size similar to Roche range of less than 40 mGal (Soderblom et al., 2015). Thus, cases for a top depth deeper than 22 km are unlikely to explain the observation.

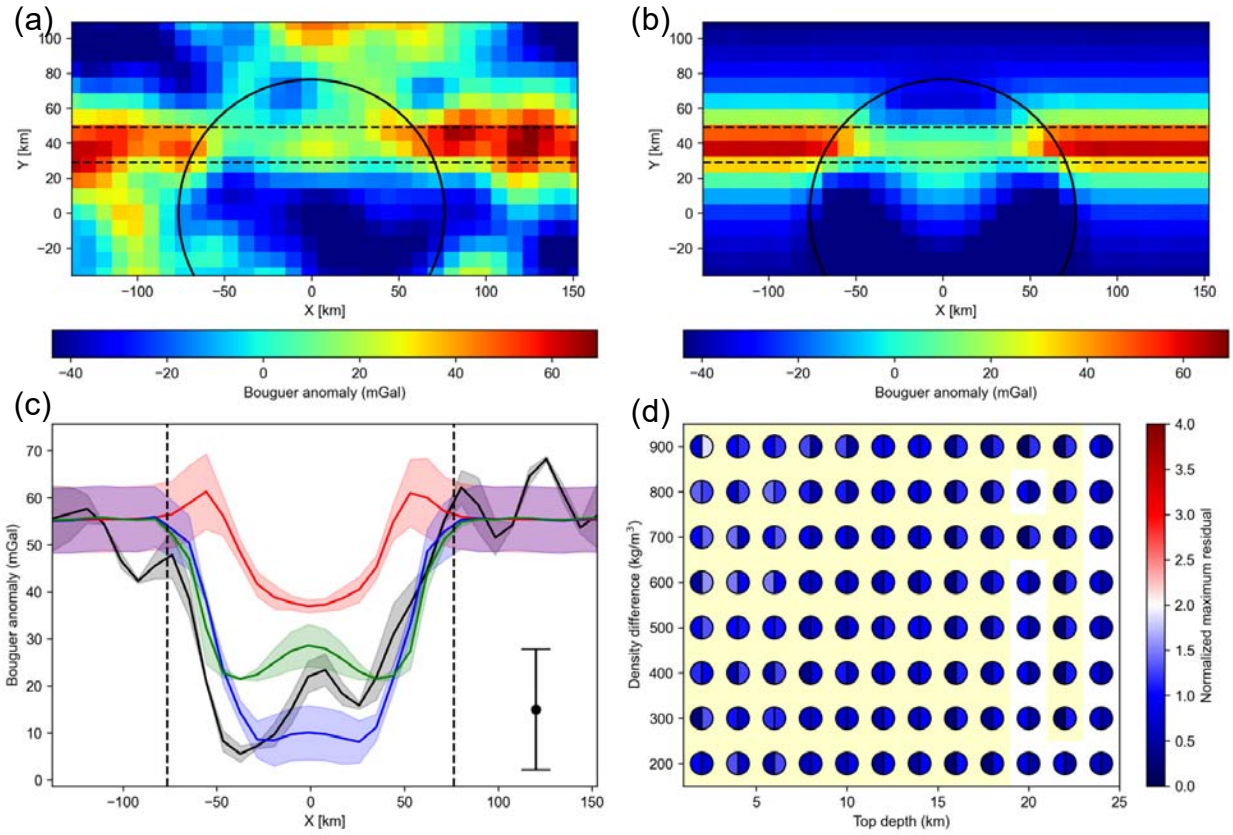

Figure 8. Comparison between simulations and the observed data. (a) The Bouguer anomaly map around Rowland crater. The solid black line shows the rim position. The area between the two black dashed lines is the area used for the comparison. (b) An example of a simulated Bouguer anomaly map when the density difference, top depth, and initial crustal porosity are assumed to be 400 kg/m^3, 10 km, and 2.0 %, respectively. (c) The averaged gravity profile within the compared area. The observed data is shown in the black line. The red, green, and blue lines show the gravity change by the LGA modification, porosity change, and the sum of these two effects. The shaded areas correspond to a standard deviation range within the compared area along the y-axis. The black error bar shows a standard deviation of the LGA gravity outside the crater. (d) The normalized difference at the local maximum and minimum within the crater. The colors in the right and left semi-circles show the values at the local minimum and maximum, respectively. The color behind the circle is yellow when the necessary gravity decrease solely from the porosity change is larger than 40 mGal.

5 Discussion on each LGA history

5.1 LGA1

The spectral and gravitational features around LGA1 imply that Rowland crater did not excavate LGA1, possibly meaning that the intrusion of LGA1 postdates the Rowland crater. As demonstrated in our gravity simulations, the observed gravity profile with the substantial gravity drop does not match the assumption that Rowland crater obliterates the pre-existing LGA1. Together with the lack of HCP exposures in the periphery, these results confirm that the magmatic intrusion of LGA1 did not exist beneath the area where Rowland crater occupies at

present. There are two possibilities attributable to our result; the Rowland crater was formed coincidently just next to the edge of LGA1, or LGA1 was formed after Rowland crater. Although the first hypothesis cannot be ruled out, the probability of such a "lucky" impact is tiny. Multiplying the highland crater density (Head et al., 2010; Heyer et al., 2023) by the area where a crater may be located with its rim overlapping the terminator of LGA1 within the gravity resolution, the expectation of the number of 160-km-sized craters in contact with LGA1 is less than 0.01. Therefore, the more plausible scenario is that the LGA1 magma started to intrude into the crust after the crater formation but terminated at the rim of Roche crater.

The termination of LGA1 at the rim of Rowland crater was perhaps caused by Rowland's topography. The orientation of dike intrusion is determined by the stress state of the media and follows the direction perpendicular to the maximum tensile stress at the time of its formation (e.g., Watanabe et al., 2002). In particular, a crater-like round depression generates a stress field in which a crack-opening direction favors a circular orientation. As the demonstration of a magma ascent beneath lunar floor-fractured craters by Michaut et al. (2020), unloading by a crater bends the trajectory of dikes beneath the crater, and magma ascends towards the rim of the above crater. In Figure 1, a negative gravity gradient of LGA does not last into the Rowland crater but curves along the rim from the terminated point. Similar ring dike structures are apparent around other impact basins like Orientale (Andrews-Hanna et al., 2018). A ring fault made by a giant basin formation is regarded as a path for magma ascent. Although the size of Rowland crater is smaller than craters accompanied by such a tectonic fault, the paleo stress field caused by Rowland's unloading could bend the direction of magma intrusion around the rim of Rowland, resulting in an abrupt termination of the LGA1 gravity signature.

The above discussion on the LGA1 formation scenario suggests a new estimate of the LGA1 formation age and, furthermore, the timing of the ancient lunar expansion. Previous works have argued that the age of LGA1 is older than the Nectarian age in various ways. Sawada et al. (2016) estimated by crater-counting that the surface age around LGA1 is $\mathbf{4.20^{+0.02}_{-0.03}}$ Ga, corresponding to pre-Nectarian age. However, their argument does not agree with the cross-cutting relationship found by our analysis, showing that the surface age on LGA1 does not represent the timing of subsurface intrusion. In addition, Liang & Andrews-Hanna (2022) argue that LGA1 is likely to postdate the Rowland formation. They attribute the apparently abrupt termination of LGA1 at Rowlands' rim to a reduction of the density contrast between the crust and LGA1 intrusion by the crater-forming shock waves, but their hypothesis is ruled out by our numerical results considering the porosity change. On the other hand, they also point out that the LGA1 gravity remains but becomes a little ambiguous beneath the Upper-Imbrium-aged Schjellerup crater. This feature is similar to our numerical simulations of crater obliteration on LGA1 and 2. Therefore, the LGA1 formation started after the Nectarian age and probably ended by the Upper-Imbrium age. This age is the youngest age estimation of LGAs on the Moon at present. From the apparent cross-cutting relationships of LGAs with two giant basins, the Crisium and South-Pole-Aitken basins, Andrews-Hanna et al. (2013) constrain that the LGAs were formed within the pre-Nectarian to early Nectarian time frame. Our analysis geologically implies that the lunar expansion accompanied by LGA formations continued even later than the Nectarian age as predicted by various thermal modeling of the Moon (U et al., 2022; Zhang et al., 2013a, 2013b).

5.2 LGA2

669 Our gravity simulation poses a constraint on the LGA2 formation age and is consistent
670 with our discovery of HCP exposures in the periphery. Consistency between our gravity
671 simulations and the observed Bouguer anomalies validates the assumption of intrusion before
672 cratering, indicating that the Roche-forming impact postdates the magmatic intrusion of LGA2.
673 Roche is a Nectarian-aged crater (Wilhelms & El-Baz, 1977), and the absolute age of a light
674 plain within it is estimated to be 3.91 Ga from the crater size-frequency distribution (Hiesinger et
675 al., 2013). Therefore, together with its formation later than the South-Pole-Aitken basin
676 (Andrews-Hanna et al., 2013), our analysis confirms that the LGA2 formation occurred within
677 the pre-Nectarian to Nectarian age. This cross-cutting relationship also agrees that the discovery
678 of HCP exposures possibly originated from ancient magma intrusion excavated by Roche crater.
679 The predicted excavation depth of Roche is about 16 km and comparable to the maximum value
680 of the preferable top depth of intrusion in our analysis. Thus, the ejecta from Roche crater could
681 contain a certain portion of LGA material. In fact, most of the discovered HCP exposures in our
682 spectral analysis are located within the continuous ejecta region (Melosh, 1989; Moore et al.,
683 1974).

684 On the other hand, the majority of non-mare HCP exposures that we found are not laid
685 within the area predicted in our axisymmetric simulations. The RGB-composite and FeO maps
686 show that the basaltic materials are identified in the northern area of Roche crater (Figures S1
687 and S3). However, the LGA materials traced in our simulation are deposited mainly in the
688 northern-eastern area. Figure 9 shows the distribution of LGA materials that are expected to
689 deposit on the surface in our simulation. Because the thickness of the top-surface mixing layer is
690 at least 1 km (Yamamoto et al., 2015), the LGA material whose final depth from the surface is 1
691 km or deeper is traced in this analysis (three red lines in Figure 9). The distribution depends on
692 the assumed density and top depth. In the case of high-density assumption, because the fitted
693 width of intrusion becomes narrow, the portion of intrusions close to the crater center decreases.
694 Due to the decrease of excavation depth with the distance from the center, the volumetric ratio of
695 excavated material is reduced for high-density cases (yellow area in Figure 9). The top depth is
696 also important because the shallower the intrusion is, the more subject to the excavation (yellow
697 lines in Figure 9). Therefore, when the shallowest and widest intrusion is assumed, the simulated
698 ejecta distribution is the broadest and covers some HCP exposures discovered around the
699 Roche's rim and at the wall of Roche-B crater. We estimated areas possibly covered by LGA-
700 containing ejecta for all the assumed parameter sets. However, the prediction does not explain
701 the whole area where the basaltic material is discovered (white crosses in Figure 9).

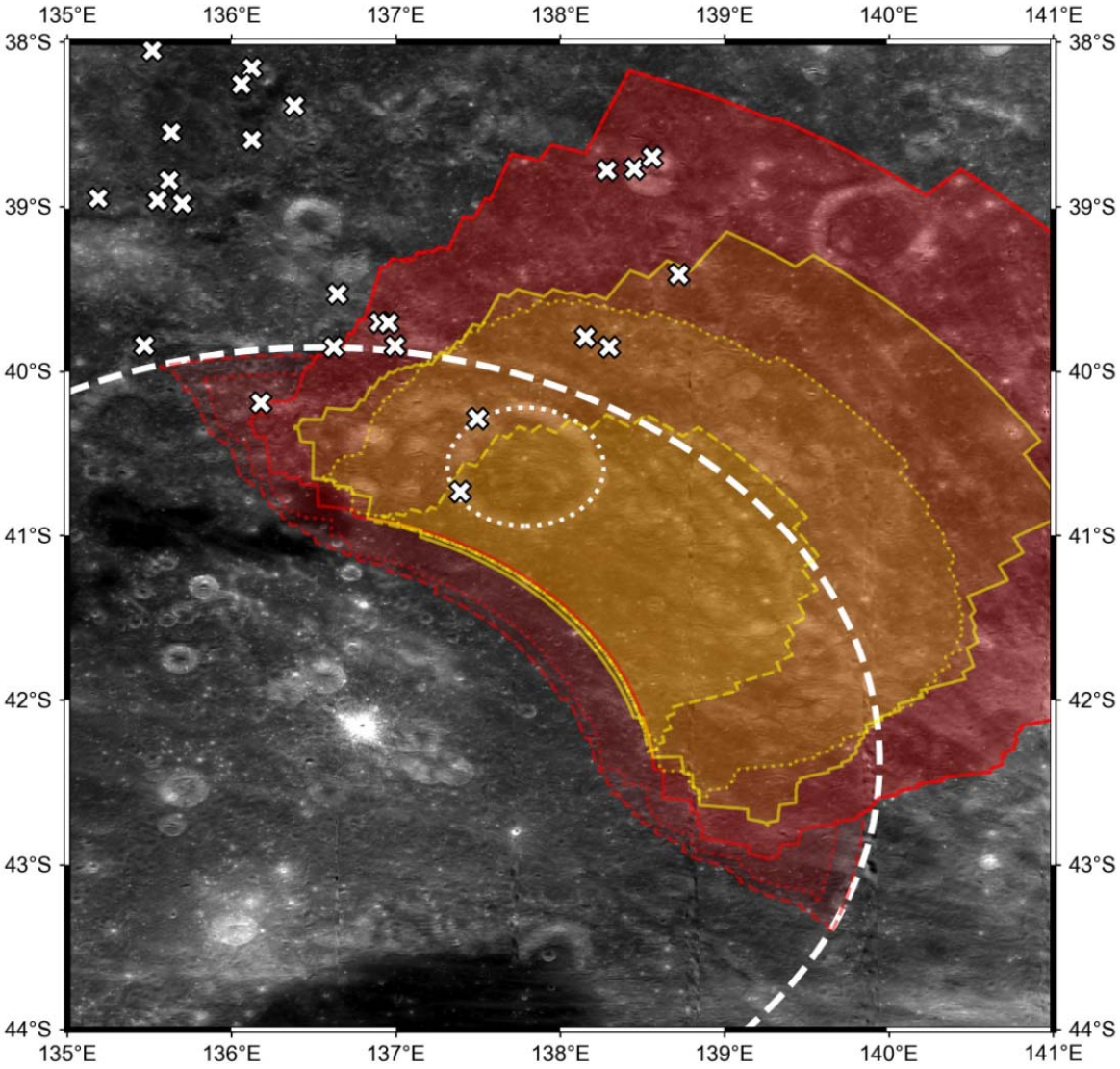

Figure 9. The deposition distribution of the LGA-containing ejecta around Roche crater. The white dashed and dotted lines show the rim of Roche and Roche B craters, respectively. The non-white lines show example distributions of ejected LGA material. The red area shows the case under the assumption of the density difference and top depth of 200 kg/m^3, 2 km, respectively. The red solid, dotted, and dashed lines show the area when the LGA tracers finally deposited at a depth shallower than 1, 2, and 3 km are considered. The yellow area shows the case with a density difference of 400 kg/m^3. The yellow solid, dotted, and dashed lines correspond to the assumed top depth of 2, 6, and 10 km, respectively. The white crosses are locations of discovered basaltic exposures flagged with E, respectively.

One hypothesis for the discrepancy between the ejecta distribution and majority of HCP exposure positions is the Roche formation by an oblique impact. Figure S7 shows the topography (SLDEM2015) around Roche crater and the highest positions in its rim. The topography data

was divided into 1-degree azimuth bins, and the highest position in each bin was extracted. To avoid contamination by ejecta from Pauli crater, the positions within its continuous ejecta region were conservatively eliminated from this analysis. After fitting an ellipse to the extracted points, we found that the Roche crater is elongated almost along the N-S direction with a semi-minor axis smaller than a semi-major axis by 7 %. According to the scaling relationships proposed by (Davison & Collins, 2022), this diameter ratio corresponds to a crater formation with an impact angle of 45 – 50 degrees. Even with such a moderate impact angle, the ejecta blankets have an asymmetry and concentrate in the impact direction (e.g., Shuvalov, 2011). Thus, the HCP discoveries centered in the northern area of Roche crater are perhaps attributed to a Roche-forming impact from the southern direction.

Another basaltic source of these HCP exposures, particularly in the case of nearby newly-identified mare patches (Figure S5), could be shallow subsurface magmatic intrusions whose spatial scale is too small to be resolved as LGA. From M^3 spectroscopy, Corley et al. (2018) have detected some olivine exposures around LGA2. However, these detections are not present at the exact location of LGA, implying that other shallow and small magmatic intrusions are exposed by impacts. Since an ascending magma is predicted to be stalled and cooled before the eruption due to the thick crust in the lunar farside (Head & Wilson, 2017; Taguchi et al., 2017; Wilson & Head, 2017), the periphery of Roche crater is possibly the case as well. In particular, the northern region of Roche crater has some small mare patches in the low topography (Figure S5) and might have experienced volcanic activity in the past. Although the ejecta from the present maria is not the source of these exposures, HCP from these small subsurface intrusions might be contained in the regolith of this region due to the later impact mixing and is exposed at the discovered points. Nevertheless, the composition of analyzed exposures should reflect that of the ancient magma, which is a hint to know the compositions of ancient subsurface intrusions.

5.3 LGA20

Contrary to LGA1 and 2, the gravity signature of LGA20 is not so obvious to discuss whether the exposure candidates were excavated by Edison crater or not. The Bouguer gradient map shows an ambiguous continuation of LGA20 into Edison crater (Figure 1f). The Bouguer anomaly value inside the crater is weaker by 20 mGal than that outside it. Although this small gravity drop can be explained solely by porosity variation induced by the crater formation, this feature is qualitatively similar to LGA2, suggesting the possibility of LGA material distribution in the periphery. Considering the shallow excavation depth of Edison crater, a top depth shallower than 6 km is necessary for the ejection of the intrusive body. The floor of Edison crater and nearby Lomonosov crater is filled with lava after their formation, meaning that magma could ascend to a depth of at least a few kilometers in this region. Thus, the LGA20 intrusion could have been stalled at a shallow subsurface and excavated by Edison crater, allowing us to detect the LGA material as HCP exposures.

Another possible source is a mixture of ancient mare material within the regolith around LGA20. Some previous works have identified a cryptomare in the southeastern area of Edison. Geologic categorization by Giguere et al. (2003) suggests that an ancient mare is covered by a light plain deposit in the Lomonosov-Fleming region. However, the area where HCP was discovered in our analysis is outside these cryptomare regions and defined as pyroclastic deposits, which is not consistent with our hyperspectral analysis. Whitten & Head (2015a)

surveyed cryptomare all over the Moon and included the area nearby the Edison in the Lomonosov-Fleming cryptomare. In the central region of this cryptomare, an 8-km crater has an obvious dark halo of ancient basalt (Giguere et al., 2003). The floor of this crater has the same elevation level as that of Edison crater. Therefore, if ancient basalt was distributed uniformly within this region before the Edison formation in the pre-Nectarian age, the ancient mare could be excavated and distributed as the HCP exposures.

6 Implications to ancient lunar magmatism

The above analysis and discussion suggest that the HCP exposures around LGA 2 and 20 contain ancient basaltic materials and possibly ejecta from the subsurface massive magmatic intrusions, enabling us to discuss the composition of magma directly related to the ancient lunar expansion. Kato et al. (2017) show that TiO_2 contents varied with the age of the mare unit in the PKT region as a consequence of magma source transition. In particular, there are mare patches younger than the excavated material around both LGAs. Therefore, a comparison of titanium contents between excavated ancient material and nearby young maria would allow us to interpret the compositional evolution of volcanism in the analyzed regions. However, the discovered HCP does not directly reflect the original composition because they are possibly contaminated by highland material, as seen in Figure 4.

In order to determine the original compositions of the HCP exposures, we correct the highland contamination by estimating the mixing ratio from FeO contents. Assuming the FeO abundances of uncontaminated mare and highland material and the TiO_2 abundance of highland material, both the highland-free TiO_2 contents of excavated basaltic material and the mixing ratio of highland are estimated from our MI data analysis. The FeO and TiO_2 contents of highland regolith are set at 4.0 and 0.3 wt %, respectively, following Giguere et al. (2003). The original FeO abundance of the HCP exposures is assumed in two ways: the average value of nearby maria or a typical value of lunar basalt of 18 wt %. The first assumption might underestimate the TiO_2 value because all the maria are contaminated by highland regolith to a certain extent. For example, the old mare inside Edison crater has an albedo higher than other maria (Figure 1), which indicates an ongoing transition from a highland-contaminated mare to a cryptomare (Giguere et al., 2003). On the other hand, the second value is higher than all the maria nearby LGAs (Figure 4) and thus gives us an upper limit of TiO_2 contents. Therefore, the original LGA composition would lie between these two estimations.

Similarly to nearby younger maria, the corrected highland-free TiO_2 contents of HCP exposures range from very-low- to low-Ti basalt, indicating a possibility of the same magma source. Figure 10 shows the mixing ratio of basaltic material and TiO_2 estimated after the removal of highland contamination. Under the second assumption of FeO abundance, the mare TiO_2 estimation is also corrected. With both the FeO assumptions, the original TiO_2 contents are always lower than 2.5 wt. % at both LGA 2 and 20. The young mare basalts are mostly distributed from 1 to 3 wt. %. It is known that lunar samples from Apollo and Luna missions show a bimodal distribution of TiO_2 contents (Neal & Taylor, 1992). All the observed values at the HCP exposures and nearby maria are in the same lower class, which consists of very-low- (<1 wt. %) or low (1–6 wt. %) TiO_2 basalt. This identical categorization of titanium contents

indicates a similar or perhaps common magma source of the LGA material (red and orange points in Figure 10) and nearby young maria (blue points in Figure 10). In addition, Figure 10 shows the similarity of TiO_2 contents between LGA2 and 20, suggesting a universal generation of low titanium magma during the lunar expansion stage. The same low-titanium basaltic material has also been observed in 2.03-Ga basalt samples brought by the Chang'E-5 mission (Li et al., 2021; Tian et al., 2021). Although there is a debate on the titanium contents of the picked basalt clasts due to their tiny size, the samples are classified as low-Ti basalts by tracking the crystallization sequence from titanium in olivine (Zhang et al., 2022).

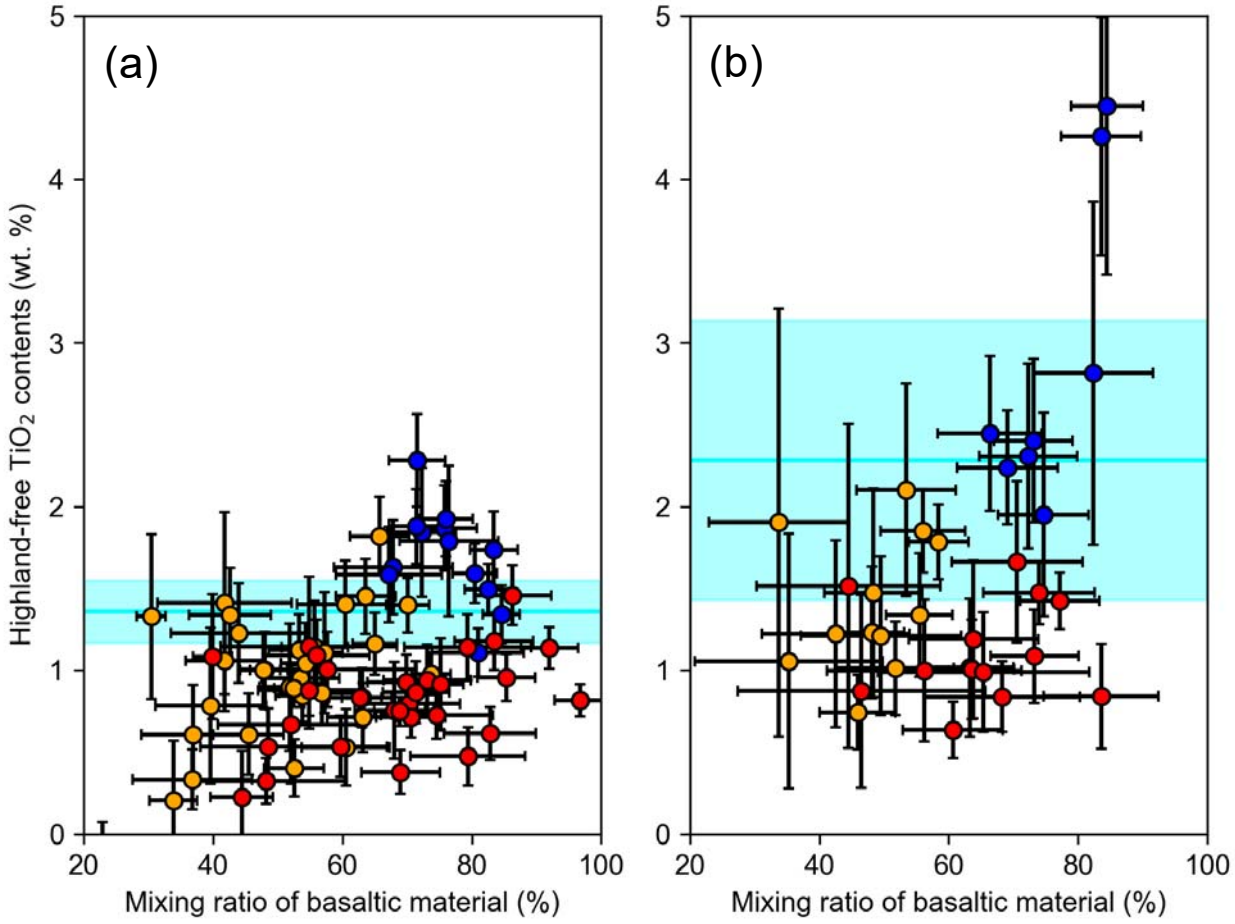

Figure 10. The corrected highland-free TiO_2 contents around (a) LGA2 and (b) LGA20. The x- and y- axes are the estimated mixing ratio of original basaltic material and highland-free TiO_2 contents in wt. %. The orange and blue points are corrected values of exposures and maria under the assumption of a typical FeO content of lunar basalt. The red points are corrected values in the use of the average FeO contents of maria within the analyzed region. The cyan lines and shades are the average and standard deviation range of the mare values without corrections.

If the magma sources for the LGA intrusion and nearby young maria are common, this tiny variation of titanium abundance implies that the magma source was compositionally almost uniform over a long period. The ages of mare patches are younger than the crater we expect to excavate the LGA materials. At LGA 2, the maria inside Roche crater has a surface age of 1.70–2.25 Ga. The absolute age of the small maria between Roche and Eotvos also ranges from 1.93 to

3.06 Ga (Pasckert et al., 2015). These mare units are younger than Roche crater, which has a light plain with an age of 3.91 Ga (Hiesinger et al., 2013). The maria around LGA 20 are categorized as units of Imbrian age (Wilhelms & El-Baz, 1977) and much younger than the pre-Nectarian-aged Edison crater. Thus, the similarity of the titanium contents between the maria and exposures implies that the composition of magma sources around these LGAs was almost uniform for 1 billion years or longer. Only a slight variation of less than 1 wt. % perhaps exists but is not so drastic as that found at the PKT region, whose TiO_2 contents increased by 2–3 wt. % around 2.3 Ga (Kato et al., 2017).

This uniform composition around LGAs also suggests a negligible mixture of a late hot plume from IBCs in the magma source region. IBCs are thought to be laid over the core-mantle boundary and/or trapped within the mantle after the lunar mantle overturn (Hess & Parmentier, 1995; Zhao et al., 2019). These IBC materials are possibly accompanied by heat-producing elements. Because the solidus of IBC is lower than that of the mantle-like olivine-orthopyroxene (Delano, 1990), IBCs could become less dense than the surrounding mantle and rise as a plume (Zhang et al., 2013a). Several numerical models have suggested that lunar hot mantle plumes from the IBC layer would happen around 2 Ga (Hess & Parmentier, 1995; de Vries et al., 2010). This mechanism has been considered as a possible source of the high-titanium magma eruption around 2 Ga, so-called Phase-2 volcanism, in the PKT region (Hiesinger et al., 2003; Kato et al., 2017; Morota et al., 2011). However, the TiO_2 variation between the LGA magma and young maria lies within 1 wt.% and is much less than that of the PKT region. This indicates that such a titanium-rich plume neither provides the young magma directly nor contaminates the magma source heavily in this farside region. Such a titanium-poor plume in the farside reflects the lunar dichotomy of IBC distribution. As seen in the Mg# (Mg/(Mg+Fe) in mole per cent) distribution (Ohtake et al., 2012), the farside crust crystallized from less-evolved magma and could lie over less IBC than the nearside crust. In addition, several numerical models have predicted that convection during the mantle overturn makes IBC material in the farside mantle less than that in the nearside mantle (Parmentier et al., 2002; Zhang et al., 2022).

7 Conclusions

To estimate the composition of magmatism during lunar ancient expansion, we investigated spectral and gravity datasets around three craters located on LGAs: Rowland crater on LGA1, Roche crater on LGA2, and Edison crater on LGA20. Although LGAs have no prominent spectral feature right above them, LGAs reduced inside these craters suggest that ancient magma could have been excavated and distributed around them. We first analyzed spectral absorption with the MI data from Kaguya and M^3 data from Chandrayaan-1 to characterize the ejecta from subsurface intrusion. Using an RGB-composite map with the absorption depth at 950, 1050, and 1250 nm, we surveyed non-mare basaltic exposures. The type of pyroxene at the discovered exposures is then examined with the MGM spectral deconvolution method. We next compared the gravity data with gravity simulated with iSALE to discuss whether the discovered exposures originate from the LGA intrusion or not. After the preparation of intrusion shape sets by fitting the gravity profile outside the crater, we numerically traced the subsurface modification, excavation, and porosity change to simulate how the pre-existing LGA is reduced by the impact.

In the case of Rowland, both the spectral and gravity analysis revealed that the LGA intrusion was not excavated by the cratering. No exposures with a clear indication of high-calcium pyroxene have been identified around Rowland crater. The simulated gravity does not match the observed gravity because the gravity signature of intrusion cannot be destroyed due to the remaining root of the LGA intrusion even after the impact. Thus, the abrupt termination of LGA at the rim of Rowland cannot be attributed to Rowland's excavation. Considering the low formation probability of a crater in contact with the LGA terminator, it is the most plausible that LGA1 formation postdates the Rowland-forming impact, indicating the lunar expansion stage lasting even after the Nectarian age.

In contrast, both Roche and Edison craters enable us to estimate the magma composition during the lunar expansion. In their peripheries, basaltic exposures are totally found at more than 40 candidates, mostly accompanied by high-calcium pyroxene. Because the possibility of exogenic contamination, such as ejecta from the mare region, is ruled out, these exposures are hypothesized to originate from the subsurface LGA intrusion. The gravity simulation with iSALE also supports this hypothesis. Although Edison crater is too small to quantify the comparison, a gravity drop similar to LGA2 inside Roche is reproduced in our modeling. In addition, some exposures are inside the ejecta blanket containing the LGA2 material. After correcting contamination by highland regolith using the FeO contents, the LGA intrusion is revealed to be composed of low-titanium magma. In particular, small young maria around LGA2 with ages of 2–3 Ga also consists of low-titanium basalt. This similarity implies that the magma source region is compositionally uniform over a long period and not contaminated by a plume from the IBC layer, perhaps reflecting the dichotomy of titanium content inside the lunar mantle.

Acknowledgments

This work was supported by the IGPEES WINGS Program of the University of Tokyo, JSPS KAKENHI Grant Number JP22J12387, and JSPS Overseas Challenge Program for Young Researchers. We gratefully acknowledge the developers of iSALE-2D (https://isale-code.github.io), including Kai Wünnemann, Dirk Elbeshausen, Boris Ivanov, and Jay Melosh. We used pySALEplot to analyze the output file of iSALE and thank Tom Davison for the development of pySALEPlot. We are also grateful to Hauke Hussmann, Alexander Stark, Mark Wieczorek, Takahiro Hiroi, and Kosuke Kurosawa for fruitful discussions and helpful comments. Numerical computations were carried out on the general-purpose PC cluster at the Center for Computational Astrophysics, National Astronomical Observatory of Japan. Numerical

analyses were carried out on the analysis servers at the Center for Computational Astrophysics, National Astronomical Observatory of Japan.

Open Research

All the MI datasets can be downloaded via the SELENE data archive system in the Data ARchives and Transmission System (DARTS) of JAXA (https://darts.isas.jaxa.jp/planet/pdap/selene/). The M3 datasets are stored in the PDS Imaging Node (https://pds-imaging.jpl.nasa.gov/data/m3/). All the topography and gravity data (SLDEM2015 and GRGM1200A_BOUGUER) can be downloaded via the PDS Geoscience Node (https://pds-geosciences.wustl.edu). At present, the iSALE shock physics hydrocode is not fully open source, but an application for the use of iSALE may be made through https://isale-code.github.io.

References

Amsden, A. A., Ruppel, H. M., & Hirt, C. W. (1980). SALE: A Simplified ALE computer program for fluid flow at all speeds. *Los Alamos National Laboratories Report*, *LA-8095*(June), 101p. Retrieved from http://www.iaea.org/inis/collection/NCLCollectionStore/_Public/11/571/11571883.pdf?origin=publication_detail

Andrews-Hanna, J. C., Asmar, S. W., Head, J. W., Kiefer, W. S., Konopliv, A. S., Lemoine, F. G., et al. (2013). Ancient igneous intrusions and early expansion of the moon revealed by GRAIL gravity gradiometry. *Science*, *339*(6120), 675–678. https://doi.org/10.1126/science.1231753

Andrews-Hanna, J. C., Head, J. W., Johnson, B. C., Keane, J. T., Kiefer, W. S., McGovern, P. J., et al. (2018). Ring faults and ring dikes around the Orientale basin on the Moon. *Icarus*, *310*, 1–20. https://doi.org/10.1016/j.icarus.2017.12.012

Barker, M. K., Mazarico, E., Neumann, G. A., Zuber, M. T., Haruyama, J., & Smith, D. E. (2016). A new lunar digital elevation model from the Lunar Orbiter Laser Altimeter and SELENE Terrain Camera. *Icarus*, *273*, 346–355. https://doi.org/10.1016/j.icarus.2015.07.039

Besse, S., Sunshine, J., Staid, M., Boardman, J., Pieters, C., Guasqui, P., et al. (2013). A visible and near-infrared photometric correction for Moon Mineralogy Mapper (M3). *Icarus*, *222*(1), 229–242. https://doi.org/10.1016/j.icarus.2012.10.036

Besse, S., Sunshine, J. M., & Gaddis, L. R. (2014). Volcanic glass signatures in spectroscopic survey of newly proposed lunar pyroclastic deposits. *Journal of Geophysical Research: Planets*, *119*(2), 355–372. https://doi.org/10.1002/2013JE004537

Boardman, J. W., Pieters, C. M., Green, R. O., Lundeen, S. R., Varanasi, P., Nettles, J., et al. (2011). Measuring moonlight: An overview of the spatial properties, lunar coverage, selenolocation, and related Level 1B

products of the Moon Mineralogy Mapper. *Journal of Geophysical Research: Planets*, *116*(6), 1–15. https://doi.org/10.1029/2010JE003730

Bottke, W. F., Vokrouhlický, D., Minton, D., Nesvorný, D., Morbidelli, A., Brasser, R., et al. (2012). An Archaean heavy bombardment from a destabilized extension of the asteroid belt. *Nature*, *485*(7396), 78–81. https://doi.org/10.1038/nature10967

Clark, R. N., Pieters, C. M., Green, R. O., Boardman, J. W., & Petro, N. E. (2011). Thermal removal from near-infrared imaging spectroscopy data of the Moon. *Journal of Geophysical Research: Planets*, *116*(6), 1–9. https://doi.org/10.1029/2010JE003751

Cloutis, E. A., & Gaffey, M. J. (1991). Pyroxene spectroscopy revisited: spectral-compositional correlations and relationship to geothermometry. *Journal of Geophysical Research*, *96*(E5). https://doi.org/10.1029/91je02512

Collins, G. S. (2014). Numerical simulations of impact crater formation with dilatancy. *Journal of Geophysical Research: Planets*, *119*(12), 2600–2619. https://doi.org/10.1002/2014JE004708

Collins, G. S., Melosh, H. J., & Wünnemann, K. (2011). Improvements to the ε-α Porous compaction model for simulating impacts into high-porosity solar system objects. *International Journal of Impact Engineering*, *38*(6), 434–439. https://doi.org/10.1016/j.ijimpeng.2010.10.013

Collins, Gareth S., Melosh, H. J., & Ivanov, B. A. (2004). Modeling damage and deformation in impact simulations. *Meteoritics and Planetary Science*, *39*(2), 217–231. https://doi.org/10.1111/j.1945-5100.2004.tb00337.x

Corley, L. M., McGovern, P. J., Kramer, G. Y., Lemelin, M., Trang, D., Gillis-Davis, J. J., et al. (2018). Olivine-bearing lithologies on the Moon: Constraints on origins and transport mechanisms from M3 spectroscopy, radiative transfer modeling, and GRAIL crustal thickness. *Icarus*, *300*, 287–304. https://doi.org/10.1016/j.icarus.2017.09.012

Davison, T. M., & Collins, G. S. (2022). Complex Crater Formation by Oblique Impacts on the Earth and Moon. *Geophysical Research Letters*, *49*(21), 1–9. https://doi.org/10.1029/2022gl101117

Delano, J. W. (1990). Buoyancy-driven melt segregation in the Earth's Moon. I. Numerical results. In *Lunar and Planetary Science Conference, 20th, Houston, TX, Mar. 13-17, 1989, Proceedings (A90-33456 14-91). Houston, TX, Lunar and Planetary Institute, 1990, p. 3-12.* (Vol. 4, pp. 3–12).

Denevi, B. W., Lucey, P. G., Hochberg, E. J., & Steutel, D. (2007). Near-infrared optical constants of pyroxene as a function of iron and calcium content. *Journal of Geophysical Research*, *112*(E5), E05009. https://doi.org/10.1029/2006JE002802

Elkins-Tanton, L. T., Burgess, S., & Yin, Q. Z. (2011). The lunar magma ocean: Reconciling the solidification process with lunar petrology and geochronology. *Earth and Planetary Science Letters*, *304*(3–4), 326–336. https://doi.org/10.1016/j.epsl.2011.02.004

Giguere, T. A., Hawke, B. R., Blewett, D. T., Bussey, D. B. J., Lucey, P. G., Smith, G. A., et al. (2003). Remote sensing studies of the Lomonosov-Fleming region of the Moon. *Journal of Geophysical Research: Planets*, *108*(11). https://doi.org/10.1029/2003je002069

Green, R. O., Pieters, C., Mouroulis, P., Eastwood, M., Boardman, J., Glavich, T., et al. (2011). The Moon Mineralogy Mapper (M3) imaging spectrometer for lunar science: Instrument description, calibration, on-orbit measurements, science data calibration and on-orbit validation. *Journal of Geophysical Research: Planets*, *116*(10), 1–31. https://doi.org/10.1029/2011JE003797

Head, J. W., & Wilson, L. (2017). Generation, ascent and eruption of magma on the Moon: New insights into source depths, magma supply, intrusions and effusive/explosive eruptions (Part 2: Predicted emplacement processes and observations). *Icarus*, *283*, 176–223. https://doi.org/10.1016/j.icarus.2016.05.031

Head, J. W., Fassett, C. I., Kadish, S. J., Smith, D. E., Zuber, M. T., Neumann, G. A., & Mazarico, E. (2010). Global distribution of large lunar craters: Implications for resurfacing and impactor populations. *Science*, *329*(5998), 1504–1507. https://doi.org/10.1126/science.1195050

Hess, P. C., & Parmentier, E. M. (1995). A model for the thermal and chemical evolution of the Moon's interior: implications for the onset of mare volcanism. *Earth and Planetary Science Letters*, *134*(3–4), 501–514. https://doi.org/10.1016/0012-821X(95)00138-3

Heyer, T., Iqbal, W., Oetting, A., Hiesinger, H., van der Bogert, C. H., & Schmedemann, N. (2023). A comparative analysis of global lunar crater catalogs using OpenCraterTool – An open source tool to determine and compare crater size-frequency measurements. *Planetary and Space Science*, *231*(January), 105687. https://doi.org/10.1016/j.pss.2023.105687

Hiesinger, H., Head, J. W., Wolf, U., Jaumann, R., & Neukum, G. (2003). Ages and stratigraphy of mare basalts in Oceanus Procellarum, Mare Nubium, mare Cognitum, and Mare Insularum. *Journal of Geophysical Research: Planets*, *108*(7). https://doi.org/10.1029/2002je001985

Hiesinger, H., van der Bogert, C. H., Thiessen, F., & Robinson, M. S. (2013). Absolute Model Ages of Light Plains in the Southern Lunar Hemisphere. *Lunar and Planetary Science Conference*, 4–5.

Isaacson, P. J., Pieters, C. M., Besse, S., Clark, R. N., Head, J. W., Klima, R. L., et al. (2011). Remote compositional analysis of lunar olivine-rich lithologies with Moon Mineralogy Mapper (M3) spectra. *Journal of Geophysical Research: Planets*, *116*(4), 1–17. https://doi.org/10.1029/2010JE003731

Isaacson, P. J., Petro, N. E., Pieters, C. M., Besse, S., Boardman, J. W., Clark, R. N., et al. (2013). Development, importance, and effect of a ground truth correction for the Moon Mineralogy Mapper reflectance data set. *Journal of Geophysical Research: Planets*, *118*(3), 369–381. https://doi.org/10.1002/jgre.20048

Ivanov, B. A., Deniem, D., & Neukum, G. (1997). Implementation of dynamic strength models into 2D hydrocodes: Applications for atmospheric breakup and impact cratering. *International Journal of Impact Engineering*, *20*(1–5), 411–430. https://doi.org/10.1016/s0734-743x(97)87511-2

Kato, S., Morota, T., Yamaguchi, Y., Watanabe, S. I., Otake, H., & Ohtake, M. (2017). Magma source transition of lunar mare volcanism at 2.3 Ga. *Meteoritics and Planetary Science*, *52*(9), 1899–1915. https://doi.org/10.1111/maps.12896

Kiefer, W. S., MacKe, R. J., Britt, D. T., Irving, A. J., & Consolmagno, G. J. (2012). The density and porosity of lunar rocks. *Geophysical Research Letters*, *39*(7). https://doi.org/10.1029/2012GL051319

Klima, R. L., Pieters, C. M., & Dyar, M. D. (2007). Spectroscopy of synthetic Mg-Fe pyroxenes I: Spin-allowed and spin-forbidden crystal field bands in the visible and near-infrared. *Meteoritics and Planetary Science*, *42*(2), 235–253. https://doi.org/10.1111/j.1945-5100.2007.tb00230.x

Klima, R. L., Dyar, M. D., & Pieters, C. M. (2011). Near-infrared spectra of clinopyroxenes: Effects of calcium content and crystal structure. *Meteoritics and Planetary Science*, *46*(3), 379–395. https://doi.org/10.1111/j.1945-5100.2010.01158.x

Krüger, T., van der Bogert, C. H., & Hiesinger, H. (2016). Geomorphologic mapping of the lunar crater Tycho and its impact melt deposits. *Icarus*, *273*, 164–181. https://doi.org/10.1016/j.icarus.2016.02.018

Kumaresan, P. R., & Saravanavel, J. (2022). Compositional Mapping and Spectral Analysis of Sulpicius Gallus Dark Mantling Deposits Using Lunar Orbital Data Sets Including Chandrayaan-1 Moon Mineralogy Mapper. *Journal of the Indian Society of Remote Sensing*, *50*(7), 1301–1319. https://doi.org/10.1007/s12524-022-01529-4

Laneuville, M., Wieczorek, M. A., Breuer, D., & Tosi, N. (2013). Asymmetric thermal evolution of the Moon. *Journal of Geophysical Research: Planets*, *118*(7), 1435–1452. https://doi.org/10.1002/jgre.20103

Lemoine, F. G., Goossens, S., Sabaka, T. J., Nicholas, J. B., Mazarico, E., Rowlands, D. D., et al. (2014). GRGM900C: A degree 900 lunar gravity model from GRAIL primary and extended mission data. *Geophysical Research Letters*, *41*(10), 3382–3389. https://doi.org/10.1002/2014GL060027

Li, Q. L., Zhou, Q., Liu, Y., Xiao, Z., Lin, Y., Li, J. H., et al. (2021). Two-billion-year-old volcanism on the Moon from Chang'e-5 basalts. *Nature*, *600*(7887), 54–58. https://doi.org/10.1038/s41586-021-04100-2

Liang, W., & Andrews-Hanna, J. C. (2022). Probing the source of ancient linear gravity anomalies on the Moon. *Icarus*, *380*. https://doi.org/10.1016/j.icarus.2022.114978

Liu, T., Luther, R., Manske, L., & Wünnemann, K. (2022). Melt Production and Ejection From Lunar Intermediate-Sized Impact Craters: Where Is the Molten Material Deposited? *Journal of Geophysical Research: Planets*, *127*(8), 1–13. https://doi.org/10.1029/2022JE007264

Lucey, P. G., Taylor, G. J., Hawke, B. R., & Spudis, P. D. (1998). FeO and TiO 2 concentrations in the South Pole-Aitken basin: Implications for mantle composition and basin formation. *Journal of Geophysical Research: Planets*, *103*(E2), 3701–3708. https://doi.org/10.1029/97JE03146

Lucey, P. G., Blewett, D. T., Taylor, G. J., & Hawke, B. R. (2000). Imaging of lunar surface maturity. *Journal of Geophysical Research: Planets*, *105*(E8), 20377–20386. https://doi.org/10.1029/1999JE001110

Lucey, P. G., Blewett, D. T., & Jolliff, B. L. (2000). Lunar iron and titanium abundance algorithms based on final processing of Clementine ultraviolet-visible images. *Journal of Geophysical Research: Planets*, *105*(E8), 20297–20305. https://doi.org/10.1029/1999JE001117

Lucey, P. G., Norman, J. A., Crites, S. T., Taylor, G. J., Hawke, B. R., Lemelin, M., & Melosh, H. J. (2014). A large spectral survey of small lunar craters: Implications for the composition of the lunar mantle. *American Mineralogist*, *99*(11–12), 2251–2257. https://doi.org/10.2138/am-2014-4854

McGetchin, T. R., Settle, M., & Head, J. W. (1973). Radial Thickness Variation in Impact Crater Ejecta :, *20*, 226–236.

Melosh, H. J. (1989). *Impact cratering : a geologic process*. New York ; Oxford: Oxford University Press ; Clarendon Press. Retrieved from http://www.loc.gov/catdir/enhancements/fy0638/88005353-t.html

1042 Melosh, H. J., Ryan, E. V., & Asphaug, E. (1992). Dynamic fragmentation in impacts: Hydrocode simulation of
1043 laboratory impacts. *Journal of Geophysical Research*, *97*(E9), 14735. https://doi.org/10.1029/92JE01632
1044 Melosh, H. J., Freed, A. M., Johnson, B. C., Blair, D. M., Andrews-Hanna, J. C., Neumann, G. A., et al. (2013). The
1045 origin of lunar mascon basins. *Science*, *340*(6140), 1552–1555. https://doi.org/10.1126/science.1235768
1046 Michaut, C., Pinel, V., & Maccaferri, F. (2020). Magma ascent at floor-fractured craters diagnoses the lithospheric
1047 stress state on the Moon. *Earth and Planetary Science Letters*, *530*, 115889.
1048 https://doi.org/10.1016/j.epsl.2019.115889
1049 Milbury, C., Johnson, B. C., Melosh, H. J., Collins, G. S., Blair, D. M., Soderblom, J. M., et al. (2015). Preimpact
1050 porosity controls the gravity signature of lunar craters. *Geophysical Research Letters*, *42*(22), 9711–9716.
1051 https://doi.org/10.1002/2015GL066198
1052 Miljković, K., Wieczorek, M. A., Laneuville, M., Nemchin, A., Bland, P. A., & Zuber, M. T. (2021). Large impact
1053 cratering during lunar magma ocean solidification. *Nature Communications*, *12*(1), 1–18.
1054 https://doi.org/10.1038/s41467-021-25818-7
1055 Miljković, Katarina, Wieczorek, M. A., Collins, G. S., Solomon, S. C., Smith, D. E., & Zuber, M. T. (2015).
1056 Excavation of the lunar mantle by basin-forming events on the Moon. *Earth and Planetary Science Letters*,
1057 *409*, 243–251. https://doi.org/10.1016/j.epsl.2014.10.041
1058 Moore, H. J., Hodges, C. A., & Scott, D. H. (1974). Multiringed basins - Illustrated by Orientale and associated
1059 features. *Proc. Lunar Sci. Conf. 5th.*, *1*, 71–100.
1060 Moriarty, D. P., & Pieters, C. M. (2018). The Character of South Pole-Aitken Basin: Patterns of Surface and
1061 Subsurface Composition. *Journal of Geophysical Research: Planets*, *123*(3), 729–747.
1062 https://doi.org/10.1002/2017JE005364
1063 Morota, T., Haruyama, J., Ohtake, M., Matsunaga, T., Honda, C., Yokota, Y., et al. (2011). Timing and
1064 characteristics of the latest mare eruption on the Moon. *Earth and Planetary Science Letters*, *302*(3–4), 255–
1065 266. https://doi.org/10.1016/j.epsl.2010.12.028
1066 Neal, C. R., & Taylor, L. A. (1992). Petrogenesis of mare basalts: A record of lunar volcanism. *Geochimica et*
1067 *Cosmochimica Acta*, *56*(6), 2177–2211. https://doi.org/10.1016/0016-7037(92)90184-K
1068 Ogawa, Y., Matsunaga, T., Nakamura, R., Saiki, K., Ohtake, M., Hiroi, T., et al. (2011). The widespread occurrence
1069 of high-calcium pyroxene in bright-ray craters on the Moon and implications for lunar-crust composition.
1070 *Geophysical Research Letters*, *38*(17). https://doi.org/10.1029/2011GL048569
1071 Ohtake, M., Haruyama, J., Matsunaga, T., Kodama, S., Morota, T., & Yokota, Y. (2008). Scientific objectives and
1072 specification of the SELENE Multiband Imager. *Advances in Space Research*, *42*(2), 301–304.
1073 https://doi.org/10.1016/j.asr.2007.04.041
1074 Ohtake, M., Pieters, C. M., Isaacson, P., Besse, S., Yokota, Y., Matsunaga, T., et al. (2013). One Moon, Many
1075 Measurements 3: Spectral reflectance. *Icarus*, *226*(1), 364–374. https://doi.org/10.1016/j.icarus.2013.05.010
1076 Ohtake, M., Uemoto, K., Yokota, Y., Morota, T., Yamamoto, S., Nakamura, R., et al. (2014). Geologic structure
1077 generated by large-impact basin formation observed at the South Pole-Aitken basin on the Moon. *Geophysical*
1078 *Research Letters*, *41*(8), 2738–2745. https://doi.org/10.1002/2014GL059478
1079 Ohtake, Makiko, Takeda, H., Matsunaga, T., Yokota, Y., Haruyama, J., Morota, T., et al. (2012). Asymmetric
1080 crustal growth on the Moon indicated by primitive farside highland materials. *Nature Geoscience*, *5*(6), 384–
1081 388. https://doi.org/10.1038/ngeo1458
1082 Otake, H., Ohtake, M., & Hirata, N. (2012). Lunar Iron and Titanium Abundance Algorithms Based on SELENE
1083 (Kaguya) Multiband Imager Data (p. 1905). Texas: 43rd Lunar and Planetary Science Conference.
1084 Parmentier, E. M., Zhong, S., & Zuber, M. T. (2002). Gravitational differentiation due to initial chemical
1085 stratification: origin of lunar asymmetry by the creep of dense KREEP? *Earth and Planetary Science Letters*,
1086 *201*(3–4), 473–480. https://doi.org/10.1016/S0012-821X(02)00726-4
1087 Pasckert, J. H., Hiesinger, H., & van der Bogert, C. H. (2015a). Small-scale lunar farside volcanism. *Icarus*, *257*,
1088 336–354. https://doi.org/10.1016/j.icarus.2015.04.040
1089 Pasckert, J. H., Hiesinger, H., & van der Bogert, C. H. (2015b). Small-scale lunar farside volcanism. *Icarus*, *257*,
1090 336–354. https://doi.org/10.1016/j.icarus.2015.04.040
1091 Pieters, C. M., Goswami, J. N., Clark, R. N., Annadurai, M., Boardman, J., Buratti, B., et al. (2009). Character and
1092 spatial distribution of OH/H2O on the surface of the moon seen by M3 on chandrayaan-1. *Science*, *326*(5952),
1093 568–572. https://doi.org/10.1126/science.1178658
1094 Piskorz, D., & Stevenson, D. J. (2014). The formation of pure anorthosite on the Moon. *Icarus*, *239*, 238–243.
1095 https://doi.org/10.1016/j.icarus.2014.06.015

Sato, H., Robinson, M. S., Lawrence, S. J., Denevi, B. W., Hapke, B., Jolliff, B. L., & Hiesinger, H. (2017). Lunar mare TiO2 abundances estimated from UV/Vis reflectance. *Icarus*, *296*, 216–238. https://doi.org/10.1016/j.icarus.2017.06.013

Sawada, N., Morota, T., Kato, S., Ishihara, Y., & Hiramatsu, Y. (2016). Constraints on timing and magnitude of early global expansion of the Moon from topographic features in linear gravity anomaly areas. *Geophysical Research Letters*, *43*(10), 4865–4870. https://doi.org/10.1002/2016GL068966

Shuvalov, V. (2011). Ejecta deposition after oblique impacts: An influence of impact scale. *Meteoritics and Planetary Science*, *46*(11), 1713–1718. https://doi.org/10.1111/j.1945-5100.2011.01259.x

Snyder, G. A., Taylor, L. A., & Neal, C. R. (1992). A chemical model for generating the sources of mare basalts: Combined equilibrium and fractional crystallization of the lunar magmasphere. *Geochimica et Cosmochimica Acta*, *56*(10), 3809–3823. https://doi.org/10.1016/0016-7037(92)90172-F

Soderblom, J. M., Evans, A. J., Johnson, B. C., Melosh, H. J., Miljkovic, K., Phillips, R. J., et al. (2015). The fractured Moon: Production and saturation of porosity in the lunar highlands from impact cratering. *Geophysical Research Letters*, *42*(17), 6939–6944. https://doi.org/10.1002/2015GL065022

Sunshine, J. M., Pieters, C. M., & Pratt, S. F. (1990). Deconvolution of mineral absorption bands: an improved approach. *Journal of Geophysical Research*, *95*(B5), 6955–6966. https://doi.org/10.1029/JB095iB05p06955

Taguchi, M., Morota, T., & Kato, S. (2017). Lateral heterogeneity of lunar volcanic activity according to volumes of mare basalts in the farside basins. *Journal of Geophysical Research: Planets*, *122*(7), 1505–1521. https://doi.org/10.1002/2016JE005246

Tian, H. C., Wang, H., Chen, Y., Yang, W., Zhou, Q., Zhang, C., et al. (2021). Non-KREEP origin for Chang'e-5 basalts in the Procellarum KREEP Terrane. *Nature*, *600*(7887), 59–63. https://doi.org/10.1038/s41586-021-04119-5

U, K., Hasumi, H., & Ogawa, M. (2022). Effects of magma-generation and migration on the expansion and contraction history of the Moon. *Earth, Planets and Space*, *74*(1). https://doi.org/10.1186/s40623-022-01631-4

de Vries, J., van den Berg, A., & van Westrenen, W. (2010). Formation and evolution of a lunar core from ilmenite-rich magma ocean cumulates. *Earth and Planetary Science Letters*, *292*(1–2), 139–147. https://doi.org/10.1016/j.epsl.2010.01.029

Wang, Y., Wu, B., Xue, H., Li, X., & Ma, J. (2021). An Improved Global Catalog of Lunar Impact Craters (≥1 km) With 3D Morphometric Information and Updates on Global Crater Analysis. *Journal of Geophysical Research: Planets*, *126*(9), 1–25. https://doi.org/10.1029/2020JE006728

Watanabe, T., Masuyama, T., Nagaoka, K., & Tahara, T. (2002). Analog experiments on magma-filled cracks: Competition between external stresses and internal pressure. *Earth, Planets and Space*, *54*(12), 1247–1261. https://doi.org/10.1186/bf03352453

Whitten, J., & Head, J. (2015a). Lunar cryptomaria: Physical characteristics, distribution, and implications for ancient volcanism. *Icarus*, *247*, 150–171. https://doi.org/10.1016/j.icarus.2014.09.031

Whitten, J., & Head, J. W. (2015b). Lunar cryptomaria: Mineralogy and composition of ancient volcanic deposits. *Planetary and Space Science*, *106*, 67–81. https://doi.org/10.1016/j.pss.2014.11.027

Wilhelms, D. E., & El-Baz, F. (1977). *Geologic map of the east side of the Moon*. *IMAP*. https://doi.org/10.3133/i948

Wilson, L., & Head, J. W. (2017). Generation, ascent and eruption of magma on the Moon: New insights into source depths, magma supply, intrusions and effusive/explosive eruptions (Part 1: Theory). *Icarus*, *283*, 146–175. https://doi.org/10.1016/j.icarus.2015.12.039

Wünnemann, K., Collins, G. S., & Melosh, H. J. (2006). A strain-based porosity model for use in hydrocode simulations of impacts and implications for transient crater growth in porous targets. *Icarus*, *180*(2), 514–527. https://doi.org/10.1016/j.icarus.2005.10.013

Yamamoto, S., & Watanabe, S. (2021). Characterization of D-Type Spectra Based on Hyperspectral Remote Sensing of the Lunar Surface. *Journal of Geophysical Research: Planets*, *126*(1). https://doi.org/10.1029/2020JE006669

Yamamoto, S., Nakamura, R., Matsunaga, T., Ogawa, Y., Ishihara, Y., Morota, T., et al. (2015). Global occurrence trend of high-Ca pyroxene on lunar highlands and its implications. *Journal of Geophysical Research: Planets*, *120*(5), 831–848. https://doi.org/10.1002/2014JE004740

Yamamoto, S., Watanabe, S., & Matsunaga, T. (2018). Space-Weathered Anorthosite as Spectral D-Type Material on the Martian Satellites. *Geophysical Research Letters*, *45*(3), 1305–1312. https://doi.org/10.1002/2017GL076612

Yokota, Y., Matsunaga, T., Ohtake, M., Haruyama, J., Nakamura, R., Yamamoto, S., et al. (2011). Lunar photometric properties at wavelengths 0.5-1.6μm acquired by SELENE Spectral Profiler and their dependency on local albedo and latitudinal zones. *Icarus*, *215*(2), 639–660. https://doi.org/10.1016/j.icarus.2011.07.028

Zhang, D., Su, B., Chen, Y., Yang, W., Mao, Q., & Jia, L. H. (2022, April 1). Titanium in olivine reveals low-Ti origin of the Chang'E-5 lunar basalts. *Lithos*. Elsevier B.V. https://doi.org/10.1016/j.lithos.2022.106639

Zhang, N., Parmentier, E. M., & Liang, Y. (2013a). A 3-D numerical study of the thermal evolution of the Moon after cumulate mantle overturn: The importance of rheology and core solidification. *Journal of Geophysical Research: Planets*, *118*(9), 1789–1804. https://doi.org/10.1002/jgre.20121

Zhang, N., Parmentier, E. M., & Liang, Y. (2013b). Effects of lunar cumulate mantle overturn and megaregolith on the expansion and contraction history of the Moon. *Geophysical Research Letters*, *40*(19), 5019–5023. https://doi.org/10.1002/grl.50988

Zhang, Nan, Ding, M., Zhu, M. H., Li, H., Li, H., & Yue, Z. (2022). Lunar compositional asymmetry explained by mantle overturn following the South Pole–Aitken impact. *Nature Geoscience*, *15*(1), 37–41. https://doi.org/10.1038/s41561-021-00872-4

Zhao, Y., de Vries, J., van den Berg, A. P., Jacobs, M. H. G., & van Westrenen, W. (2019). The participation of ilmenite-bearing cumulates in lunar mantle overturn. *Earth and Planetary Science Letters*, *511*, 1–11. https://doi.org/10.1016/j.epsl.2019.01.022

Zuber, M. T., Smith, D. E., Watkins, M. M., Asmar, S. W., Konopliv, A. S., Lemoine, F. G., et al. (2013). Gravity field of the moon from the Gravity Recovery and Interior Laboratory (GRAIL) mission. *Science*, *339*(6120), 668–671. https://doi.org/10.1126/science.1231507